

(Univ. Prof. Dr. Friedrich Aumayr)



TECHNISCHE
UNIVERSITÄT
WIEN

DIPLOMARBEIT

Coincidence Measurements of Ion-Induced Electron Emission from Graphene

Ausgeführt am Institut für
Angewandte Physik
der Technischen Universität Wien
Wiedner Hauptstraße 8-10 / 134
1040 Wien

unter der Anleitung von
Univ.-Prof. Dr. Friedrich AUMAYR

durch

Janine SCHWESTKA
Matrikelnummer 1025552
Stuckgasse 14/8
1070 Wien

Wien, 30. März 2016

Janine Schwestka

Abstract

With its unique properties, single layer graphene (SLG) has been considered as an outstanding candidate for many possible future applications in nano-electronics as well as in ultrafiltration. This has triggered considerable interest in the investigation of its electronic structure, and possibilities to modify this structure, e.g. by ion impact, have been investigated. In this connection collision studies with ions and the resulting electron emission can help to improve the understanding of interaction processes between charged projectiles and this ultimately thin 2D material.

In this thesis ion-induced electron emission from freestanding SLG is investigated. A new experimental setup for detecting emitted electrons in coincidence with ions traversing through the graphene has been built. Thin carbon foils, single layer graphene and its Quantifoil support have been bombarded with slow multiply charged Ar^{q+} ions ($2 \leq q \leq 9$) with impact energies ≤ 54 keV to determine the number statistics of emitted electrons. An evaluation routine is implemented enabling a routine calculation of the total emission yield. For obtaining the emission statistics non-negligible electron backscattering from the detector surface and various background contributions are taken into account.

To gain access to contributions by kinetic and potential electron emission, measurements with varying projectile velocities and charge states are performed. A linear dependence of the electron emission yield on the ion impact velocity is found for graphene and amorphous carbon. The obtained data are compared with emission yields from highly ordered pyrolytic graphite (HOPG). The dependence on the ion charge state is observed by bombarding the examined targets with argon ions at a fixed impact energy. As expected a strong dependence on the projectile charge state is shown for all these carbon-based materials pointing to a dominant potential emission process. For bombardment with multiply charged ions SLG is found to have a higher electron emission yield compared to amorphous carbon.

Within the scope of this thesis the Quantifoil support, on which the graphene is mounted, was found to be not sufficiently thick to stop Ar projectiles at these impact energies. Coincidence measurements of ion-induced electron emission are therefore not able to separate electrons originating from SLG and those from SLG on Quantifoil support. A possible solution for this problem is suggested in the Outlook of this work.

Kurzfassung

Mit seinen einzigartigen Eigenschaften wird monolagiges Graphen schon jetzt als hervorragender Kandidat für zukünftige Anwendungen gesehen. Dies hat in den letzten Jahren zu einer Vielzahl an Untersuchungen der elektronischen Struktur von Graphen geführt. Wechselwirkungsprozesse mit Ionen und die dabei resultierende Elektronenemission soll einen tieferen Einblick in mögliche Modifizierungen genau dieser Struktur geben und vor allem dabei helfen, die zugrundeliegenden Wechselwirkungsprozesse zwischen geladenen Teilchen und diesen ultimativ dünnen Materialien zu verstehen.

Im Rahmen dieser Diplomarbeit wurde Ionen-induzierte Elektronenemission aus freistehendem Graphen untersucht und zu diesem Zwecke eine neue Messapparatur aufgebaut. Diese ermöglicht es, emittierte Elektronen in Koinzidenz mit den entsprechenden Ionen zu detektieren, die die Monolage aus Graphen durchqueren. Langsame mehrfach geladene Ar^{q+} -Ionen ($2 \leq q \leq 9$) mit Energien unterhalb von 54 keV werden zur Kollision mit dem genannten Graphen und weiteren Materialien, wie dünnen Kohlenstofffolien und dem Trägermaterial Quantifoil, gebracht. Daraus ließ sich eine statistische Verteilung der im Mittel emittierten Elektronen gewinnen. Außerdem wurde ein Auswerteprogramm implementiert, welches unter Berücksichtigung von Elektronenrückstreuung von der Detektoroberfläche und diversen Untergrundbeiträgen die Bestimmung der totalen Elektronenemission ermöglicht.

Messungen mit variierenden Projektilgeschwindigkeiten wurden durchgeführt, um einen umfassenderen Zugang zu den Beiträgen der kinetischen Emission wie auch der Potentialemission zu erlangen. Eine lineare Abhängigkeit der beobachteten Elektronenemission von der Aufprallgeschwindigkeit der Ionen konnte sowohl für Graphen als auch für die amorphen Kohlenstoff Folien gezeigt werden. In guter Übereinstimmung können die erhaltenen Daten mit jenen für Elektronenemission von HOPG (Highly Ordered Pyrolytic Graphite) verglichen werden. Des Weiteren wurde die Abhängigkeit der Ausbeute an emittierten Elektronen vom Ladungszustand des eintreffenden Ions für eine fixe Projektil-Energie bestimmt. Wie es für die hier dominante Potentialemission zu erwarten ist, zeigte sich eine starke Abhängigkeit vom Ladungszustand des Ions für alle untersuchten Kohlenstoff-basierten Materialien. Es ist eindeutig zu erkennen, dass Graphen, verglichen mit einer um einiges dickeren Kohlenstofffolie, beim Beschuss mit mehrfach geladenen Ionen eine höhere Elektronenemission aufweist.

Als wichtiges Resultat stellte sich heraus, dass das Trägermaterial Quantifoil nicht dick genug ist, um die einfallenden Argon-Ionen zu stoppen. Koinzidenzmessungen für Ionen-induzierte Elektronenemission sind daher derzeit nicht in der Lage, emittierte Elektronen von freistehendem Graphen von jenen zu separieren, die von Graphen auf dem Trägermaterial stammen. Eine Möglichkeit dieses Manko zu beheben, wird im Ausblick dieser Arbeit vorgestellt.

Contents

1	Introduction	1
1.1	Motivation	1
1.2	Ion-induced electron emission from surfaces	2
1.2.1	General theoretical concept	2
1.2.2	Classical over-barrier model	9
1.2.3	Potential electron emission	10
1.2.4	Kinetic electron emission	11
2	Experimental methods	15
2.1	Ion source	15
2.2	Ion beam formation	16
2.3	Collision chamber	18
2.3.1	Microchannel plate detector	20
2.3.2	Passivated implanted planar silicon detector	22
2.4	Examined target materials	24
2.4.1	Single layer graphene and its support	24
2.4.2	Thin carbon foils	27
2.5	Electronics and data acquisition	30
2.6	Coincidence measurements	31
2.6.1	Ion signal creating the gate	32
2.6.2	Delayed electron signal	32
2.7	Measuring procedure	33
2.7.1	Determination of the operating point	33
2.7.2	Settings for coincidence measurements	33
2.7.3	Calibration	34
3	Evaluation concept	37
3.1	Electron emission statistics	37
3.2	Yield calculation for received EES spectra	40
4	Results & Discussion	51
4.1	Coincidence spectra in comparison to non-coincidence measurements	51
4.2	Comparison of electron yields for ion bombardment of SLG and C-foils	56

4.2.1	Dependence on the projectile velocity	58
4.2.2	Charge state dependency	63
5	Conclusion & Outlook	69
	References	74
	Danksagung	83

1 Introduction

1.1 Motivation

The interaction of highly charged ions (HCI) with solid surfaces has been a much researched topic in the last years due to the wide range of possible applications. One reason for the attempt to understand the underlying physical processes is well-grounded in plasma physics, where HCI largely contribute to plasma wall interactions [1–3]. Furthermore highly charged ions find their application in nano-electronics as, for example, in semiconductor technology, where the ability for structuring surfaces at the nano-scale can be of great interest. Since its discovery [4] single layer graphene (SLG), a thin membrane made of sp^2 -hybridized carbon atoms with unique electronic properties, has been considered as an excellent candidate for these future nano-electronics. Moreover, the outstanding property of allowing water to pass while being almost completely impervious to liquids and gases [5] lead very recently to new ideas of using graphene as an ultrafiltration medium, acting as a barrier between two substances [6–8]. Finally, with the access to this ultimately thin 2D materials, interaction studies between highly charged ions and freestanding SLG become of genuine interest, because they bridge the gap between atomic collisions in gaseous and those in solid targets.

A frequent consequence of inelastic ion-surface collisions is the emission of electrons, which is an important key for a detailed understanding of the relevant processes in these interactions (e.g. [9, 10]). There one commonly distinguishes between the kinetic electron emission (KE) [11, 12], which arises as a result of the energy and momentum transfer from the projectile to the target atoms, and the potential electron emission (PE) [13–16], resulting from the conversion of internal energy stored in the impinging ion via Auger-type processes.

In the past a lot of investigations on kinetic and potential electron emission from metal [17–20] and insulator [21, 22] surfaces have been carried out at TU Wien. To bridge the mentioned gap between the interaction of highly charged ions with solid and gaseous targets a new experimental setup for electron emission measurements from SLG was designed. Due to the lack of free standing graphene targets, a concept for detecting the emitted electrons in coincidence with the transmitted slow multiply charged Ar^{q+} ions was drafted.

In the following, a short overview of ion-induced electron emission from surfaces is given. In Chapter 2 the used experimental methods are introduced while Chapter 3 describes the evaluation concept for determining the electron yield. Chapter 4 presents the obtained results from these coincidence measurements. Conclusions and outlook are announced in Chapter 5.

1.2 Ion-induced electron emission from surfaces

1.2.1 General theoretical concept

When slow ions impinge on solid surfaces a multitude of phenomena, which are of great interest in plasma physics, surface-analytics, -preparation and -modification as well as in related applications, can be observed. The resulting interaction processes depend on the properties of the target material as, for example, the electronic structure, transport processes, the work function and the surface topography. On the other hand, the arising phenomena in these particle-surface interactions are also affected by the potential and kinetic energy of the impinging ion.

A frequent consequence of inelastic collisions between slow ions and surfaces is the emission of electrons, which are often accompanied by other processes like energy loss and backscattering of the projectile. Electron emission from surfaces can also result from the bombardment of the solid with other particles like photons or electrons but in this work only ion-induced electron emission is investigated.

Commonly, the electron emission is distinguished into two regimes. There is on the one hand the kinetic electron emission, which results from the momentum and energy transfer of the projectile to a target electron, and on the other hand the potential electron emission, arising as a consequence of the initially stored energy in the ion converted into electronic excitation of the target and causing emission of slow electrons. Extensive reviews on KE can be found in [12] and on PE in [13].

PE starts already before the ion impacts on the target, and arises from fast electronic transitions from the surface into empty projectile states. Slow electrons are emitted and for this process no minimum velocity is required. At higher impact velocities also kinetic electron emission leads to ejection of slow electrons from the target. Figure 1.1 presents the total electron emission yield for bombardment of a polycrystalline gold surface with neon ions. KE results from direct binary collisions of the projectile with target electrons. These are promoted towards the surface due to electron-electron interaction and might be emitted from the target if they have sufficient energy to overcome the surface potential barrier. The dashed line in Figure 1.1 demonstrates the theoretical velocity threshold for kinetic electron emission due to direct momentum transfer [23]. By cause of other KE mechanism like electron pro-

motion the actual KE threshold can be somewhat lower (as seen from the $q=1$ curve in Figure 1.1). Below the kinetic emission threshold potential electron emission is the only possible mechanism.

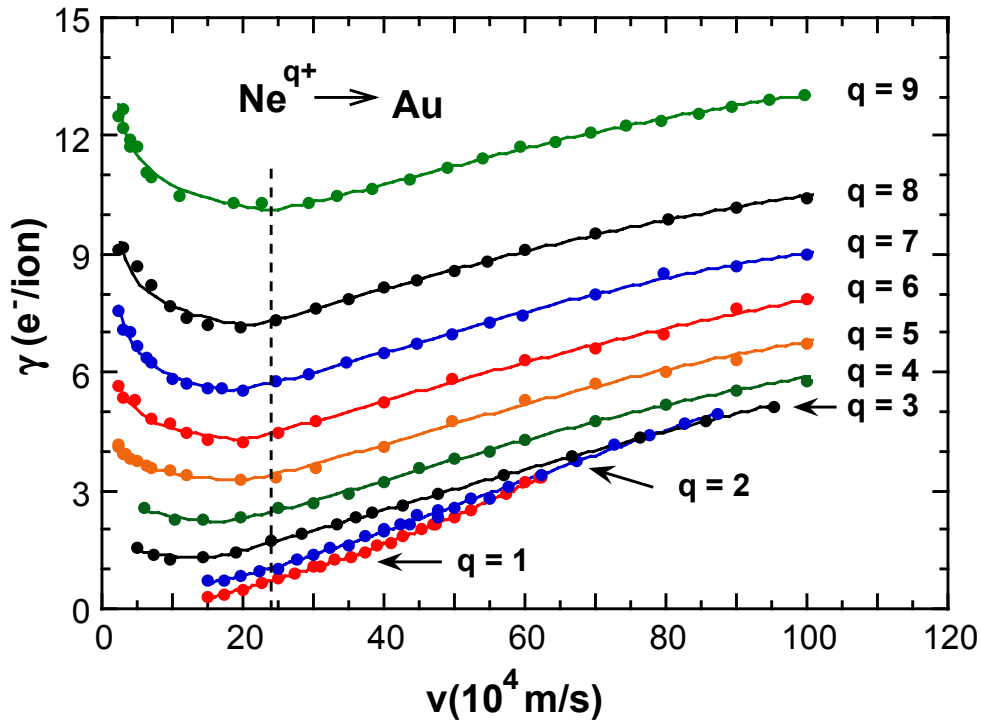


Figure 1.1: Total electron emission yield originating from both potential and kinetic emission vs impact velocity for differently charged neon ions impinging on a polycrystalline gold target. This figure is taken from [24]. The dashed line presents the theoretically calculated velocity threshold for KE due to direct momentum transfer [23].

For a complete separation of these two regimes it would be necessary to have slow ions at very high charge states (dominant PE), very slow projectiles with velocities below the KE threshold (pure PE) or neutral projectiles in their ground state (pure KE). In interaction processes where neither contribution is negligible the coincident measurement of electron emission and projectile energy loss can present a convenient instrument to separate kinetic and potential electron emission yields [25]. Varying parameters like incident energy and impact angle also provide a deeper insight due to the different influences on the emission yield for KE compared to PE [26].

Further information can also be gained by observing ion-induced electron emission from different target materials. By investigating conducting surfaces in comparison to

insulators an ample parameter range for work function and energy band gap is given. While the interaction processes of multiply charged ions (MCI) with metals are well understood, there is still a lack of experimental data for PE and KE from insulating surfaces. Due to the wide electronic band gap, different dielectric response and the charging-up of the target surface, the knowledge on ion-induced electron emission from metal surfaces cannot be extrapolated to the ones from insulators.

Slow electron emission has been analyzed in connection with kinetic energy loss, exit charge state and outgoing trajectories of the ion, as well as in conjunction with fast Auger electrons and soft x-rays emitted from the projectile after the surface impact. A general review on interaction of slow HCI with solid surfaces has been given in [27]. It summarizes our understanding of HCI-surface collisions, which can be described within the so-called hollow atom (HA) scenario [28].

When a HCI is approaching a target surface, it starts to feel its own image charge while it is accelerated towards the solid. This results in a lower limit for the effective projectile impact velocity and an upper limit for the interaction time above the solid surface. Within a critical distance the neutralization process of the projectile starts when electrons from the target are captured into highly excited (Rydberg) states of the ion. This causes the formation of a transient multiple-excited projectile which carries empty inner shells and is therefore called hollow atom [13, 27, 28].

The subsequent de-excitation of this short-lived inversion via various electronic transitions leads to the decay of the hollow atom with decreasing distance to the target. As a result a large number of low energy electrons is emitted above the surface.

When the HA approaches the surface more closely, the screening of the surface electron gas becomes dominant and all loosely bound electrons of the hollow atom are peeled off. Due to the image charge acceleration the time for a complete de-excitation is not sufficient and so the relaxation of the hollow atom proceeds inside the solid. There the remaining inner shell vacancies of the strongly screened HA recombine, resulting in the emission of a sequence of fast Auger electrons and x-rays [13, 27, 28]. Slow electrons reveal information on the situation of HA above and at the target surface, fast Auger electrons and X-rays deliver information on the HA development below the surface [27]. In Figure 1.2 a schematic overview of the different mechanisms during the hollow atom formation and decay within MCI-surface interaction is given.

Several charge exchange and relaxation processes are involved in the neutralization of a HCI. Hagstrum [14–16, 30] observed slow emitted electron yields and their energy distribution from metal surfaces. For PE he identified the four types of one- and two- electron transitions: Resonant neutralisation (RN), resonant ionisation (RI), Auger

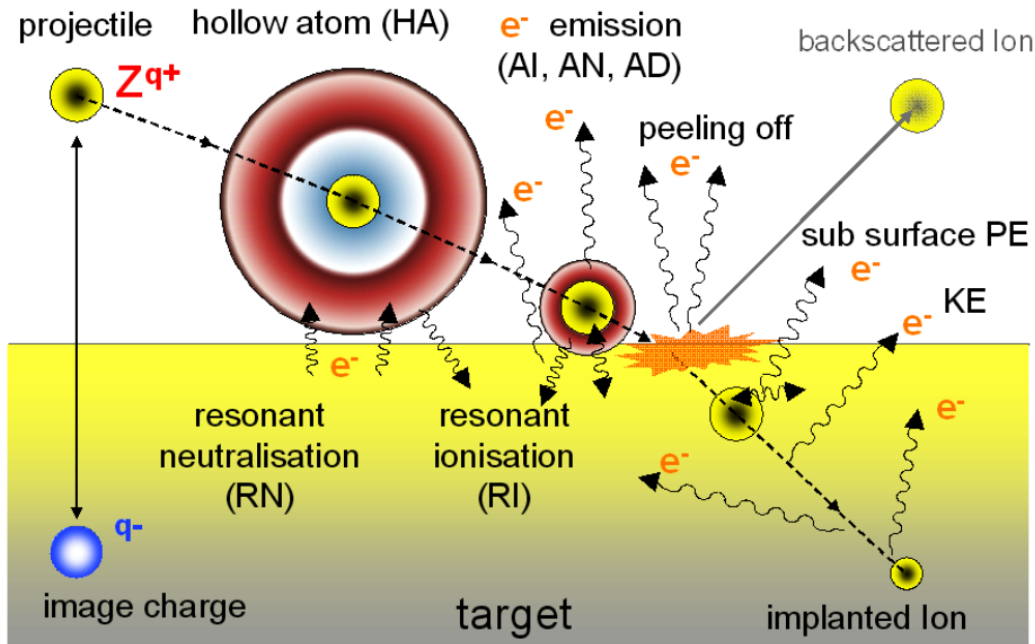


Figure 1.2: Different processes involved in hollow atom formation and -decay during MCI-surface interaction (from [29]).

neutralisation (AN) and Auger de-excitation (AD). The main processes are shortly presented in the following figures, which were taken from [29] but originally presented by [14–16, 30]. The green line indicates the potential of the solid in absence of the ion, while the red line illustrates the characteristics for both, the projectile and the target. W_ϕ depicts the target work function and E_F the Fermi energy of the solid.

Resonant electronic transitions

Resonant electronic transitions (cf. Figure 1.3) from the solid surface into excited ion states dominate the interaction between HCI and solids, due to the large spatial extension of one excited state wave function compared to one of the ground state. They do not give rise to electron emission but act as a precursor for subsequent electron-emitting processes.

Resonant neutralisation (RN) transfers an electron from the dense occupied valence band of the surface into an unoccupied state of the approaching HCI. The electron capture with the highest probability is the one into Rydberg states as a result of its large spatial extension. A sequence of RN processes generates a multiply-excited atom with empty inner shells, the hollow atom.

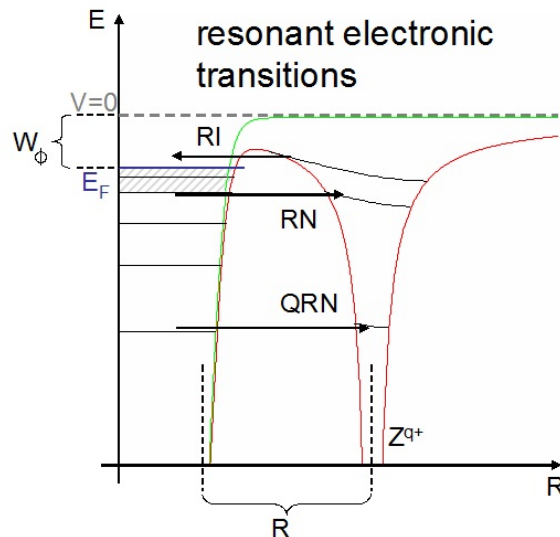


Figure 1.3: Resonant electronic transitions cause no electron emission but act as a precursor [11, 14–16, 29, 30].

Resonant ionisation (RI) is the reverse process to RN. It requires an empty level in the conduction band of the solid and a binding energy of the excited ion state smaller than the surface work function W_ϕ . Under these conditions an electron is transferred from the projectile into the empty states of the surface.

Quasi-resonant neutralisation (QRN) transfers an electron from tightly bound solid states into unoccupied low-lying projectile levels. It only occurs in sufficiently close collisions in which the overlap of inner electronic orbitals becomes noticeable. So, the closer the ion approaches the surface the more probable this transition process becomes. The resulting unoccupied state in the solid leads to fast Auger electron emission.

Auger neutralisation

Since two electrons of the solid surface are involved, the Auger neutralisation (AN) belongs to the two-electron transitions. A schematic of this process is presented in Figure 1.4. If the available potential energy W'_1 is at least twice the surface work func-

tion W_ϕ one electron can be captured by the ion and the other one can be ejected from the surface valence band with the kinetic energy

$$E_e \leq W'_i - 2 \cdot W_\phi. \quad (1.1)$$

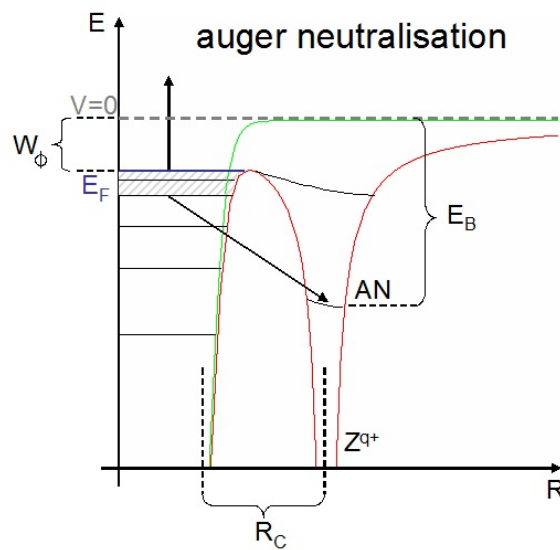


Figure 1.4: While one target electron is captured into a lower projectile state, the other one is emitted from the surface [11, 14–16, 29, 30].

Auger de-excitation

The Auger de-excitation (AD) counts also to the two-electron transitions. One electron of the solid valence band interacts with an electron of an excited ion state. If the excitation energy W_{ex} of the projectile is still larger than the surface work function W_{ϕ} the excited electron can be demoted into a lower lying state while it transfers its energy to a target electron which, as a consequence of this interaction, is ejected from the surface. In this case the remaining kinetic energy E_e of the emitted electron is given by

$$E_e \leq W_{\text{ex}} - W_{\phi}. \quad (1.2)$$

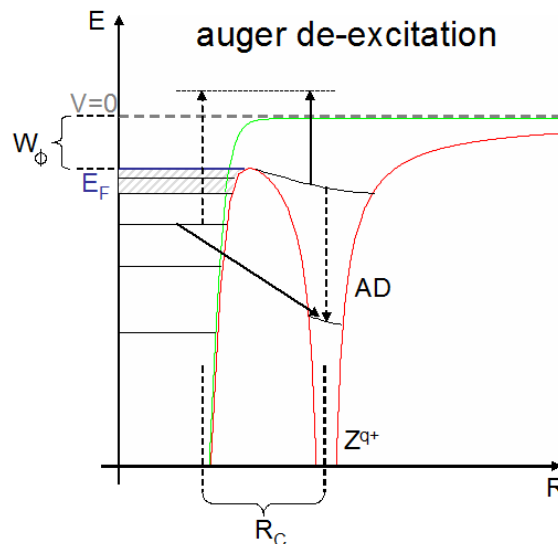


Figure 1.5: In the case of Auger de-excitation either a target electron is captured by the ion and a projectile electron is ejected or an electron from the ion is demoted while an electron is emitted from the surface [11, 14–16, 29, 30].

As it can be deduced from Figure 1.5 (solid lines) AD can also lead to the capture of a surface electron into a lower projectile state with an electron being ejected from the ion.

Auto ionisation

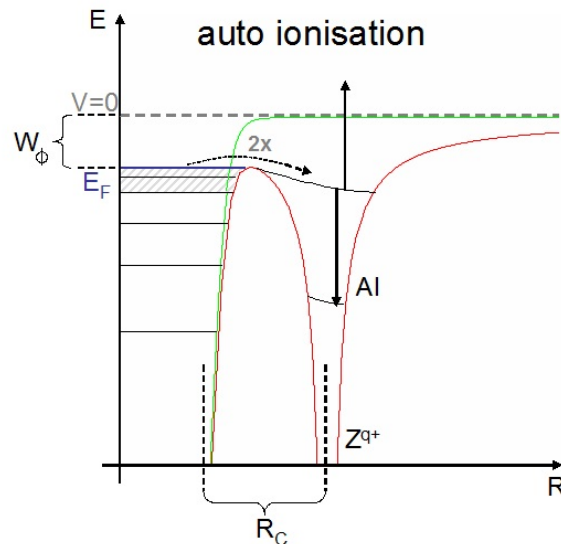


Figure 1.6: Auto ionisation represents the intra-projectile Auger de-excitation of an excited ion projectile [11, 14–16, 29, 30].

Auto ionisation (AI), presented in Figure 1.6, is the intra-projectile AD of an excited ion which requires at least two excited states of the projectile. One or more electrons are ejected into vacuum, while others in the projectile become demoted to lower states.

1.2.2 Classical over-barrier model

The classical over-barrier (COB) model describes the ion-induced electron emission above the solid surface. Originally such a model was developed for ion-atom collisions for characterizing one-electron capture into highly charged ions [31]. For including multi-electron transfer it was elaborated by [32] and [33].

Due to the requirement of describing the above-surface de-excitation and neutralization of a HCI the COB was further extended to ion-surface collisions [28]. Within

the interaction time of the projectile with the surface only classically allowed over-the-barrier processes are sufficiently fast to lead to the observed phenomena above the surface, as for example electron emission [34].

If a highly charged ion approaches the target surface, the collective response of the solid electrons for large distances can be depicted by a classical image charge attraction [35]. The target work function W_ϕ detain the electrons from leaving the solid. When the ion approaches the surface the potential barrier between the projectile and the target drops down. The COB claims that electronic transitions can only occur if the barrier falls below the Fermi level of the solid. Therefore the main parameter for potential electron emission from a solid above the surface is found in the target work function W_ϕ . The critical distance R_c , at which the ion-surface interaction processes set in, is therefore depending besides the ion charge state q also on the target work function W_ϕ [28, 36]

$$R_c = \frac{1}{2W_\phi} \sqrt{8q + 2} \approx \frac{\sqrt{2q}}{W_\phi}, \quad (1.3)$$

where the last approximation specifically pertains to HCl. As a consequence, two conducting materials with the same work function should emit a similar amount of electrons within the COB model.

The empirically found equation for the potential electron emission yield is in good agreement with the classical over-barrier model. Another important prediction is the dependence of γ_{PE} only on the perpendicular component of the ion projectile velocity, which was confirmed in many experimental works [20, 37].

The COB model was first intended for ion-metal surface interactions. Extending the description from metal to insulating targets involves several difficulties relating to the differences in the valance and conduction band structure. Compared to the conducting solids the holes in the insulators cannot be filled up as fast in insulators. Therefore investigations on the neutralization process of highly charged ions approaching a LiF surface were performed [38].

1.2.3 Potential electron emission

Charged particles carry – apart from their kinetic energy – also potential energy, which is initially stored by ionization processes, and can therefore be determined as the sum of the ionization energies. Potential electron emission is caused by the conversion of this internal projectile energy via Auger-type processes. For highly charged ions the

potential energy can surmount their kinetic energy, which can lead to a PE dominance in ion-surface interactions. PE arises at the surface impact but also above the target. The dependence of the electron yield on the projectile velocity in the case of PE was empirically derived as [19, 35, 39–41]:

$$\gamma_{PE}(v) \Big|_{\vartheta=\text{cons.}} = \gamma_{\infty} + \frac{c_v}{\sqrt{v}}, \quad (1.4)$$

where γ_{∞} can be attributed to the "peeling-off effect" [19] during the ion-surface impact. In this regime the electron yield is almost not depending on the velocity. The inverse dependence on the projectile velocity is due to the increasing interaction time in front of the surface at smaller velocities. The parameter c_v considers the auto ionization cascades in front of the surface in this collision system.

For the impact angular dependence of PE only the value of the perpendicular velocity component $v_{\perp} = v \cdot \cos(\vartheta)$ has to be taken into consideration, as it is shown in [20]. Here, the authors conclude that the PE is independent of the parallel component with respect to the surface.

As a result, the angle dependent potential electron emission follows the relation

$$\gamma_{PE}(v, \vartheta) = \gamma_{\infty} + \frac{c_v}{\sqrt{v \cdot \cos(\vartheta)}}, \quad (1.5)$$

which is in good agreement with several experimental works, in which number statistics of emitted electrons were measured as a function of the incident angle [20, 37].

1.2.4 Kinetic electron emission

As a result of surface bombardment with MCI energy is transferred from the projectile to the electronic system of the target. KE follows if the energy transfer is high enough and consequently the target work function can be overcome by the electron. Kinetically emitted electrons arise, in contrast to potential electron emission, from within the bulk and not above or at the surface. The mechanism leading to KE consist of three steps, which are well elaborated in [11]. The first one is constituted by the excitation of the electronic system. In many theories the different possible excitation mechanisms are not treated separately and therefore the generation process of electrons is considered in a semi-empirical way, in which the kinetic electron emission yield can

be approximated to be proportional to the electronic stopping power

$$S_e = \left. \frac{dE}{dx} \right|_e, \quad (1.6)$$

which is equal to the loss of energy E per unit path length x .

The second step comprises the diffusion processes transporting the electrons towards the surface. Here the excited electrons will collide with other target electrons transferring part of their energy to the latter, and thus an electron cascade will develop. The diffusion process is followed by the electron escape through the surface into the vacuum. For overcoming the surface-vacuum boundary a minimum velocity will be necessary, which leads to a velocity threshold v_{th} for kinetic electron emission due to direct momentum transfer [23]:

$$v_{th} = \frac{v_F}{2} \left(\sqrt{1 + \frac{W_\phi}{E_F}} - 1 \right) \quad (1.7)$$

where v_F is the Fermi velocity, E_F the Fermi energy and W_ϕ the target work function. The approximation is in good agreement with experimental data found in [23]. Typical threshold values are in the order of $v_{th} \approx 10^5$ m/s. Above the critical velocity the kinetic electron emission yield increases linearly with the velocity until it reaches a saturation as it is presented in [24] and can also be concluded from Figure 1.1. The linear behavior fits perfectly to the assumption that the kinetic electron emission yield γ_{KE} is proportional to the electronic stopping power

$$\gamma_{KE} = \Lambda^{ex} \left. \frac{dE}{dx} \right|_e, \quad (1.8)$$

where Λ^{ex} is just a material-dependent constant. Nevertheless, as a consequence of the generated cascades of recoil target atoms and electrons for heavy projectiles, deviation from this simple relation were found, so that γ_{KE} is more appropriately described by two separate contributions. The one part depending on the electronic stopping power is caused by the collisions between primary ions and electrons in the solid, while the other one – resulting from recoiling target atoms and electrons – is related to nuclear stopping power [42, 43]. For kinetic electron emission also the angular dependence of the yield has to be taken into consideration. For the assumption

of a straight projectile path in the target and of continuous electron excitation along this path, the total electron yield is calculated to follow an inverse cosine law [11]:

$$\gamma_{KE}(\vartheta) = \gamma(0^\circ) \cdot \cos(\vartheta)^{-1}. \quad (1.9)$$

In many experimental works, as for example in [44], the predicted angular dependence could be verified. For heavy particle projectiles, however, a deviation was observed. In [43] the KE yield dependence on the impact angle was investigated for protons, noble-gas ions and aluminum projectiles. The received results could be fitted by the function

$$\gamma_{KE}(\vartheta) = \gamma(0^\circ) \cdot \cos(\vartheta)^{-\beta}, \quad (1.10)$$

where β is a fitting parameter related to the impact energy, and varies between $0.5 \leq \beta \leq 1.5$ [11]. For high energies β approaches $\beta \rightarrow 1$.

2 Experimental methods

2.1 Ion source

For investigating ion-induced electron emission from SLG and other carbon films, Ar^{q+} projectiles within the energy range of 1 keV – 54 keV were used in this work. These slow multiply charged ions were produced by the 14.5 GHz electron cyclotron resonance ion source SOPHIE (Source for Production of Highly charged Ions using Electron cyclotron resonance) at the Institute of Applied Physics at the Vienna University of Technology. The source is capable of creating singly, as well as highly charged ions. For argon charge states of up to Ar^{14+} can be achieved [45]. An elaborated report about SOPHIE can be found in [46].

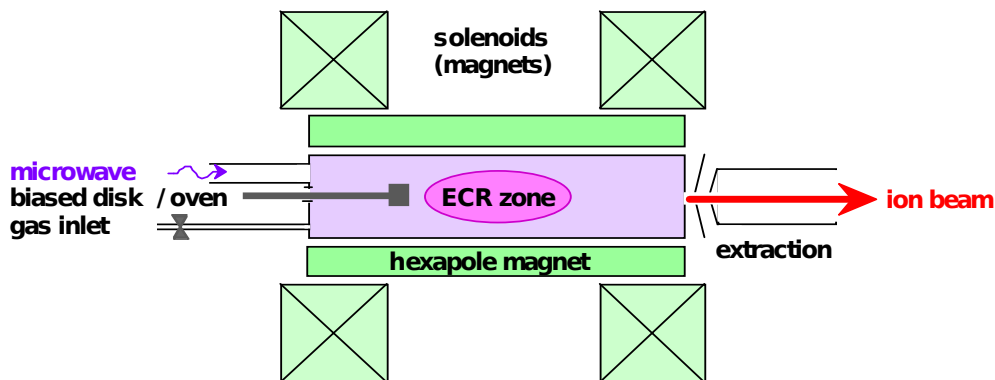


Figure 2.1: Main components of an ECRIS for production of multiply charged ions. Solenoids and multipole magnetic fields created by permanent magnets ensure the plasma confinement [46].

The main components of an electron cyclotron resonance ion source (ECRIS) are shown in Figure 2.1. The discharge chamber is filled with the working gas (pressure typically $\leq 1 \times 10^{-5}$ mbar) in which the gas atoms get ionized by collisions with electrons. The thereby created plasma is immersed in a so-called "minimum-B" magnetic field geometry, the strength of the magnetic field increases from the plasma center outwards. Due to the Lorentz force a charged particle will move in a static and uniform magnetic field in a circle, while its angular frequency will be given by

$$\omega_c = \frac{qB}{m}, \quad (2.1)$$

where B is the magnetic field, while q and m are the charge and the mass of the ion. The cyclotron motion of the electrons is used for ionizing the plasma. By absorption of injected microwaves the electrons in the plasma get heated while drifting through the so-called ECR zone. There the microwave frequency coincides with the electron cyclotron frequency ω_c according to Equation 2.1. In SOPHIE the plasma confinement is achieved by two axial and two radial permanent magnet rings and a Halbach-type hexapole magnet. The 12.75 GHz – 14.5 GHz microwaves are generated by a thin film oscillator and amplified by a solid state microwave amplifier. The plasma chamber features two separate gas inlet valves enabling the mixture of two gases, which can be beneficial for producing higher charge states.

2.2 Ion beam formation

The extraction of the ions from the plasma is accomplished in SOPHIE by a triode “accel-decel” extraction system. The outermost concentric electrode facing the plasma chamber is on source potential, the next one serves as a suppressor to keep the electrons inside the plasma chamber, and the inner electrode is on ground potential. The ion beam is accelerated from the positive plasma potential to ground potential. The system can be operated with an extraction voltage of up to 6 kV. The kinetic energy of the accelerated ions is defined by their charge state multiplied by the adjusted extraction voltage.

After the extraction system the ion beam gets focused by two magnetic quadrupoles onto the entrance of a sector magnet, where the ions are mass-to-charge m/q analyzed before the selected ion species enter one of the three beamlines. The beamline is separated from the sector magnet by a vacuum shutter valve. In between a Faraday cup for measuring the spectra of the extracted ions is arranged. In Figure 2.2 the ion beam facility with its main components at the Vienna University of Technology is presented.

Before the ions enter the experimental chamber they have to make their way through an electrostatic einzel lens, and a following pair of deflection plates (cf. Figure 2.3). The einzel lens consists of three coaxial electrically insulated cylindrical tubes, which focus the ion beam. Each cylinder can be put at a different potential to achieve the required beam focus. To conserve the ion energy tube 1 and 3 are kept at ground level, and only the second one is biased. To steer the ion beam and guide it through the

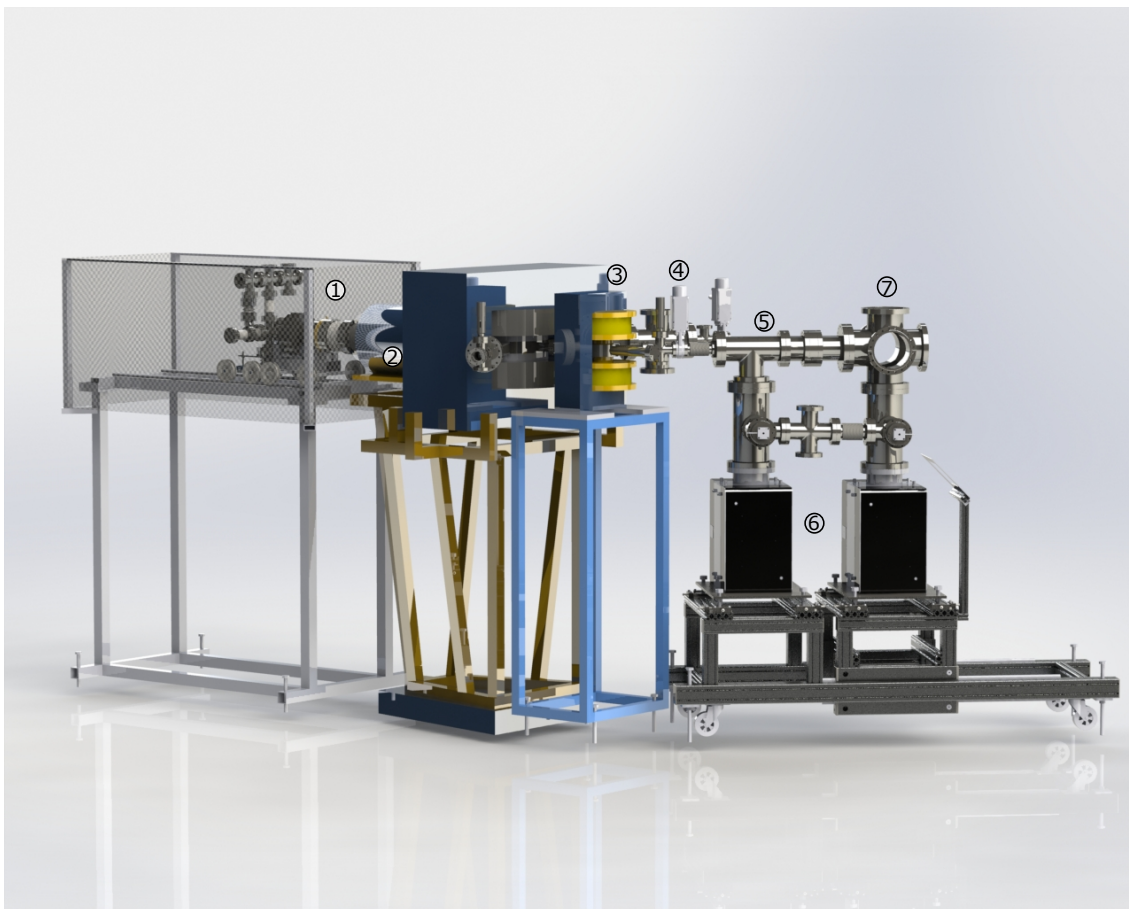


Figure 2.2: The ion beam facility at the Vienna University of Technology, including: ① the ECR ion source, ② two magnetic quadrupoles for beam focussing, ③ m/q selecting sector magnet, ④ beamline shutter with faraday cup, ⑤ einzel lens with an attached pair of deflection plates for guiding the ion beam into the target chamber, ⑥ two ion getter pumps for the required ultra high vacuum in the beamline and ⑦ the collision chamber hosting the target and the detection system

end-aperture a pair of deflection plates is attached to the end of the third tube, again electrically insulated. The deflection plates are biased at low voltages between 0 and ± 30 V.

The last beam limiting component, the end-aperture, is centered in front of the collision chamber. The original diameter of 1 mm was minimized by adding a thin metal foil with an even smaller pinhole (about 0.25 mm in diameter) for optimizing the ion beam before it hits the target. For controlling the beam parameters the aperture is insulated from the chamber and connected to a picoammeter, which realizes

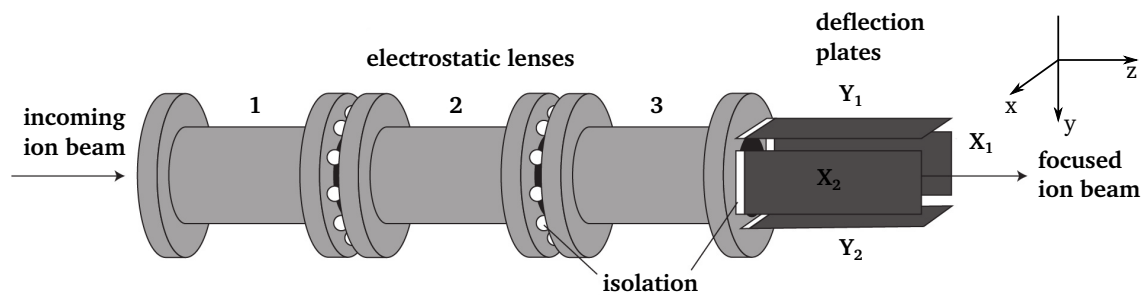


Figure 2.3: Drawing of the electrostatic einzel lens with the attached pair of deflection plates [47].

current measurements in front of the target. Nevertheless, the current deposited by impinging ions measured at the end-aperture is not the ion current that actually hits the sample, it is just proportional to the one that reaches the target. The end-aperture is surrounded by a cylindrical tube with a 3 mm orifice which serves as an electron repeller. It is negatively biased and prevents the electrons created at the end-aperture from migrating into the target chamber. Figure 2.4 presents the ion beam on its way from the extraction system of the ECRIS into the collision chamber while passing the beam focusing elements described above.

2.3 Collision chamber

To avoid neutralization of the ions on their way to the target a reasonably low pressure throughout the whole beamline including the sample chamber is needed. For this requirement two ion getter pumps reduce the pressure from 1×10^{-5} mbar in the source region to a low residual gas pressure of 1×10^{-10} mbar in the collision chamber. Figure 2.5 reveals a detailed overview of the collision chamber. After passing the end-aperture and the electron repeller the ion beam is directed onto the sample holder, where the ions finally interact with the target. Besides the purpose of holding back the negative charged particles emitted from the end-aperture, the electron repeller also serves as a focusing electrode for the electrons ejected from the sample. Being biased at -500 V for the case of an ion impact angle of 45° with respect to the impinging ions it helps to guide the emitted electrons from the interaction region in the direction of a positively biased, wired grid located in front of the detector (see Figure 2.5).

The sample carrier contains six slots for different targets and a Faraday cup in order to locate the ion beam after it passes the end-aperture. The front plate is electrically insulated from the mounting which allows the measurement of the impinging

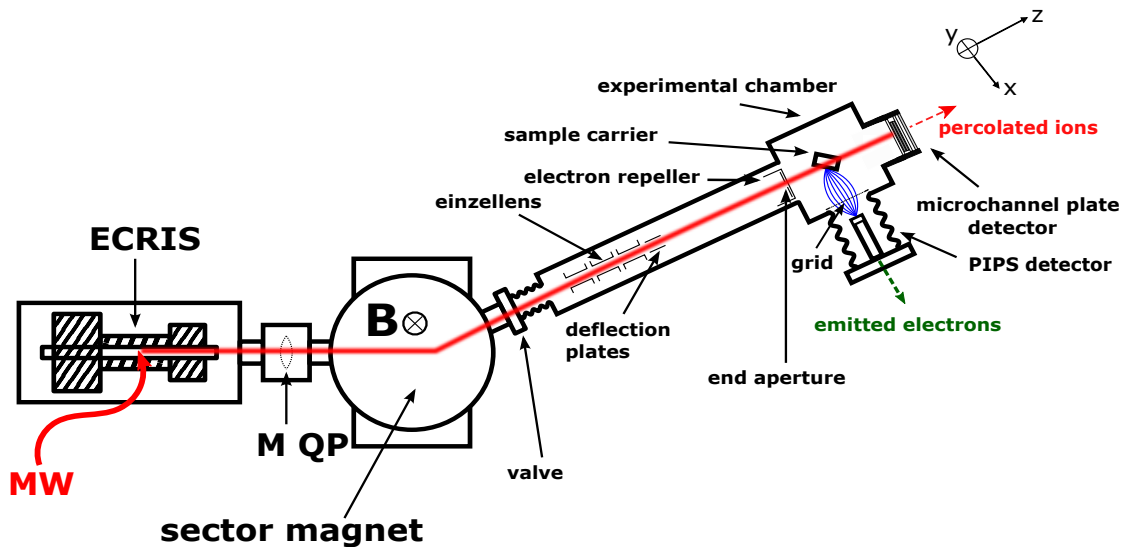


Figure 2.4: Schematic of the most important elements the ions pass on their way from the ECRIS to the target in the experimental chamber (adapted from [47]). After being focused by two magnetic quadrupoles (M QP) a specific ion species is chosen at the sector magnet and is guided into the collision chamber. An einzel lens and a pair of deflection plates steer the ion beam through the end-aperture and the electron repeller. In the experimental chamber the emitted electrons as well as the ions traversing the SLG target are detected.

ion current onto the sample carrier. A $xyz\varphi$ -manipulator enables the variation of the position as well as the impact angle (cf. Figure 2.6). For targets that allow transmission of highly charged ions, as it is the case for single layer graphene, the traversing ions are registered by a multichannel plate (MCP) detector located about 15 cm behind the target position. The electrons created in the interaction region are extracted by a weak positive electric field (210 V for an impact angle of 45° with respect to the impinging ion beam), applied to a highly transparent grid made of thin wires. Such a grid is mounted as close as possible to the target to achieve high electron collection efficiency. From the grid the electrons are accelerated onto a passivated implanted planar silicon (PIPS) detector biased at high voltage (+29 kV).

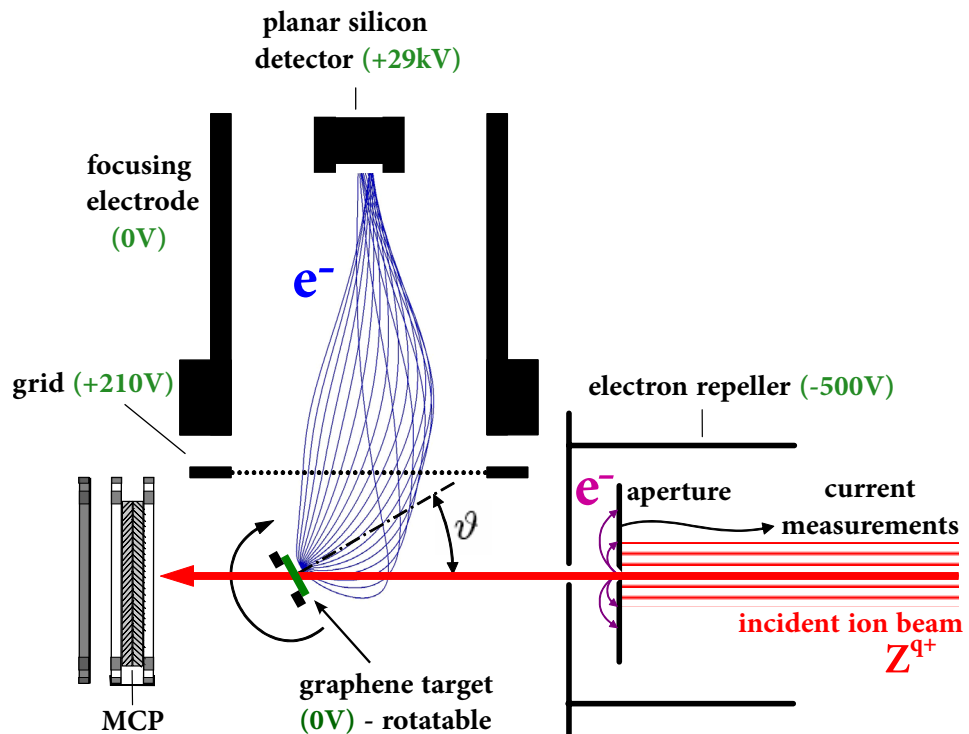


Figure 2.5: The collision chamber with the end-aperture and electron repeller at its entrance, including the target holder, the multichannel plate (MCP) for registering the traversing ions and the planar silicon detector with the positively biased grid arranged in front of it for determining the numbers statistics of emitted electrons from the SLG sample (adapted from [29]).

2.3.1 Microchannel plate detector

To perform coincidence measurements it is essential to detect the emitted electrons from the target as well as the projectiles that traverse the SLG. For this purpose a microchannel plate detector is situated behind the sample inside the experimental chamber. The electrons registered at the PIPS detector are only accepted if there is a corresponding ion impinging on the microchannel plate. The concept of the coincidence measurements is elaborated in Section 2.6.

The MCP detector, provided by RoentDek, consists of two microchannel plates made from highly resistive material, and a metal anode for detecting the output electron cloud. Each MCP is containing a large number of tiny tubes, which are covered by a material with a high secondary-electron emission coefficient in order to operate

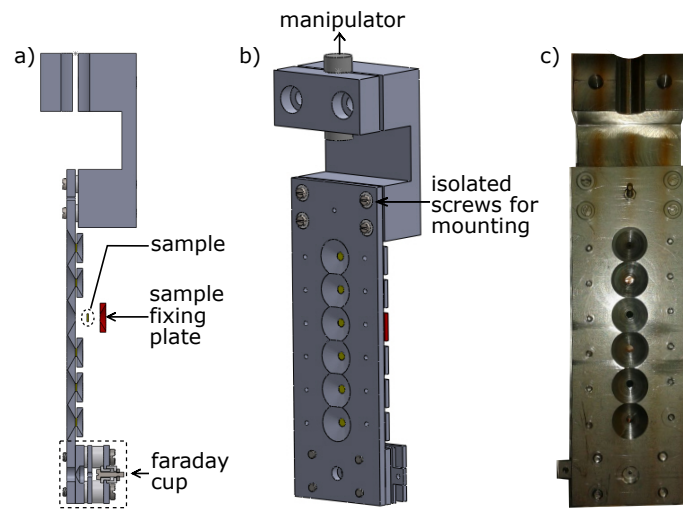


Figure 2.6: a) Central cut through the target holder and display of the sample mounting method. b) Angled view showing the connection of the holder to the manipulator. c) Picture of the completed target holder [48].

as an electron multiplier. The working principle of the MCP detector is demonstrated in Figure 2.7. If an ion impinges at the surface of the microchannel plate a number of secondary electrons are ejected. By applying an electric field between the two sides of a MCP the produced electrons are accelerated down the slot, and create a cascade of electrons along their way, which amplifies the original signal by several orders of magnitude depending on the MCP configuration and the strength of the applied electric field. The multiplied electrons exiting the channel are then detected by the metal anode.

For the measurements in this work the MCP detector was operated in the chevron configuration, as it is presented in Figure 2.7b, to reduce ion feedback in the device and to receive a higher gain at a given voltage compared to straight channel MCP.

In the used detector the set of microchannel plates is situated in front of a wedge-and-strip anode with a germanium layer in between. In this case the position sensitivity of the anode was not used but nevertheless considered as an opportunity in future investigations, where it might come to separation of ion exit charge states. By implementing deflection plates – biased at a certain voltage – in front of the MCP detector, the differently charged ions escaping the target will be focused onto different positions at the MCP. For a chevron configuration the detector can be operated at voltage differences up to 2.5 kV between the MCP-front and -back side, but sufficient gain can already be obtained at lower voltages. Therefore, in order to save the electronics from damage, the presented measurements are performed by keeping the

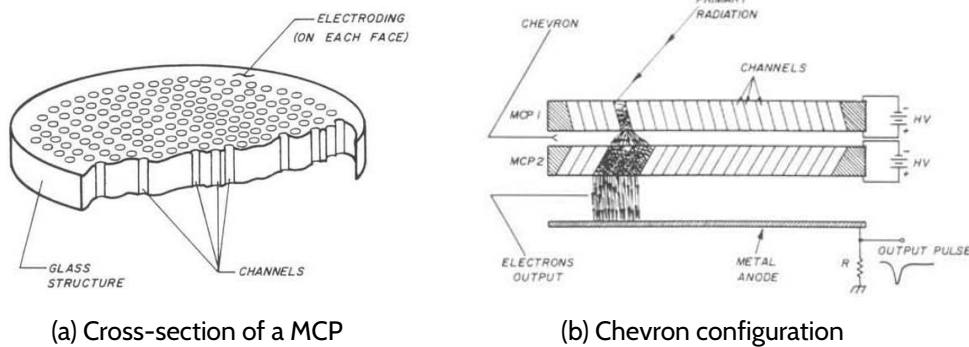


Figure 2.7: (a): Microchannel plate containing a large number of tiny channels in which the impinging particles create a cascade of secondary emitted electrons while migrating through the tubes. (b): A pair of MCP with angled channels rotated 180 degrees from each other producing a chevron shape [49].

MCP's front side at -1.7 kV and the back side at 300 V. The germanium layer, located between the microchannel plates and the anode, is kept on a slightly more positive potential (400 V) than the back side of the MCPs. It is capacitively coupled to the actual anode and enables therefore the operation of the anode on ground potential.

During operation the vacuum pressure in the chamber should never exceed 10^{-5} mbar to prevent electric discharges. Furthermore, to avoid detector damage, it is necessary to apply the voltage to the MCP in steps of 100 V.

2.3.2 Passivated implanted planar silicon detector

The unique property of the electron number statistics method to register not only the average number of electrons emitted, but also a statistical distribution of the electron emission during an ion-surface interaction process has made it to be a well-established and frequently used measuring technique for the last 25 years [17–19, 35, 50, 51].

The number of emitted electrons n induced by a single ion impact are registered simultaneously by a passivated implanted planar silicon detector, biased at high voltage U_{HV} (25 – 30 kV). The detector used in this work for the electron statistics measurements is provided by Canberra (BKPD100-12-300AM). It is situated in a grounded tube, which helps to focus the electrons onto the active area of the PIPS detector. On its inner walls the tube is highly polished to avoid field emission from tiny edges on the tube surface, which would lead to a disturbing background noise. A weak electric

field, applied to a highly transparent wired grid in front of the detector, collects the slow electrons emitted from the target (collection efficiency > 97 %). After passing the grid the electrons are further accelerated onto the detector by the high voltage potential (cf. Figure 2.8).

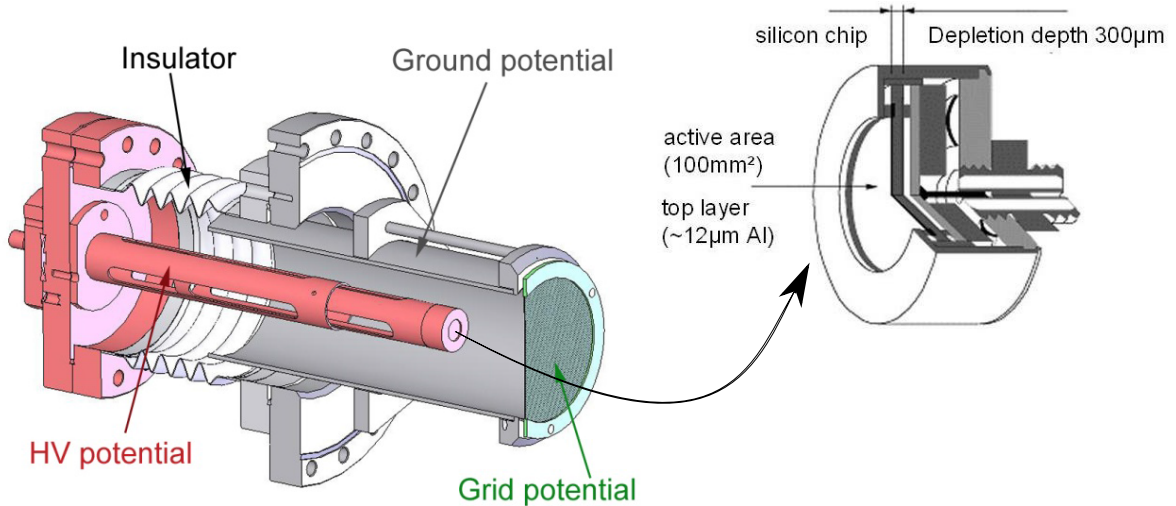


Figure 2.8: Left: PIPS detector at high voltage potential (red) in a grounded tube (grey) with a ceramic insulator keeping these two potentials apart. Highly transparent grid biased at positive voltage (green) in front of the detector is positioned as close as possible to the target for extracting the emitted electrons from the surface [52]. Right: Cutaway view of the used Canberra passivated implanted planar silicon detector [53].

The Canberra PIPS detector has a minimum depletion depth of 300 μm , and an active area of 100 mm^2 with a 12 μm aluminium layer (dead layer) on top acting as an electrode for applying the bias voltage U_{bias} (typically 50–60 V).

After passing the deadlayer the accelerated electrons deposit their energy in the active area of the detector. As a result, electron-hole pairs are created in the semiconductor material which are separated by an electric field generated by U_{bias} . This leads to a charge-pulse, in which the total charge is proportional to the deposited energy in the detector

$$E = neU_{\text{HV}}. \quad (2.2)$$

All electrons arriving within a time window of typical $1\ \mu\text{s}$ are counted in one pulse and thus, n electrons emitted due to a single projectile impact (time scale about $1 \times 10^{-12}\ \text{s}$) will be registered like one event of $n \times 25\ \text{keV}$ rather than n individual electrons with $25\ \text{keV}$. The number statistics of ion-induced electron emission can therefore be determined from the measured pulse height distribution of this measurement method. The evaluation procedure for gaining the electron emission yield will be elaborated in Chapter 3.

While traversing the deadlayer of the PIPS detector the electrons will lose already a small part of their energy, which will cause an additional broadening of the pulse height distribution due to statistical fluctuations of the energy loss. To avoid the superposition of several ion impact events (pileups), multiple projectile hits (less than $10\ \text{kHz}$) within the detector dead time have to be prohibited. Therefore one has to take care of controlling the impinging ion count rate.

2.4 Examined target materials

Before starting the coincidence measurements the electron emission statistics (EES) setup had to be optimized. Therefore the target holder was provided with samples, for which the electron yield had been already well investigated in the past ([47], [54]). A clean gold target as well as a highly ordered pyrolytic graphite (HOPG) sample were chosen in the very beginning to test the EES setup.

2.4.1 Single layer graphene and its support

After data for HOPG and Au showed that the EES branch is properly working, the actual targets of interest were mounted in the slots of the target holder. Graphene is a two-dimensional allotrope of carbon atoms with an atomic-scale honeycomb structure. It plays an important role for understanding electronic properties of other allotropes like fullerenes, graphite and carbon nano-tubes. With its unique properties graphene captured the attention of scientists all over the world. These properties include an incredible flexibility, superb conductivity, ultra-light weight, almost evanescent thickness but nevertheless being immensely tough and 100 times stronger than steel. An overview of the unique electronic properties of graphene can be found in [55] while Figure 2.9 shows its honeycomb structure.

The most important reason for performing coincidence measurements in the case of single layer graphene is due to the inevitable support on which this two-dimensional material is always attached to. A 300-mesh gold transmission electron microscopy (TEM) grid (2.7 mm in diameter) with an additional 'Quantifoil' support on top, with even smaller holes, carries the SLG sample. According to the manufacturer [56] this supporting substrate arises by evaporating polyvinyl formal (formvar) with carbon and

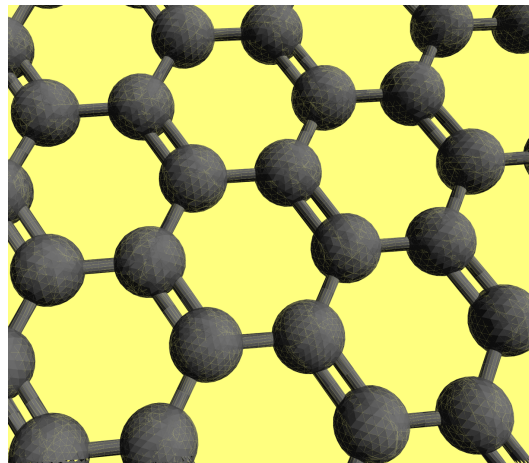
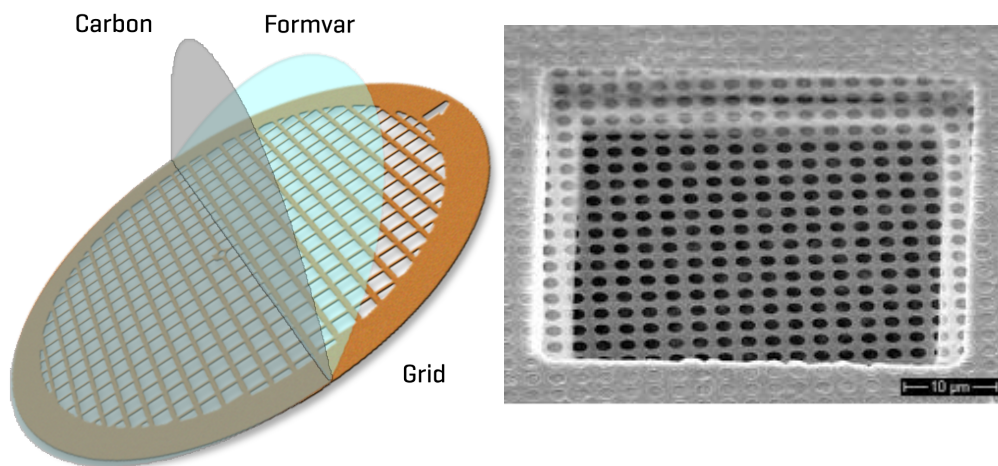


Figure 2.9: Graphene shows a two-dimensional, atomic-scale, honeycomb lattice of carbon atoms.

subsequently dissolving the thermoplastic resins. Since the total elimination of the formvar cannot be achieved a 20 nm thick holey Quantifoil remains from which only half of it consists of carbon. With a hole diameter of $1.2\ \mu\text{m}$ with a spacing of $1.3\ \mu\text{m}$ the Quantifoil, shown in Figure 2.10, is suitable for carrying the fragile SLG.



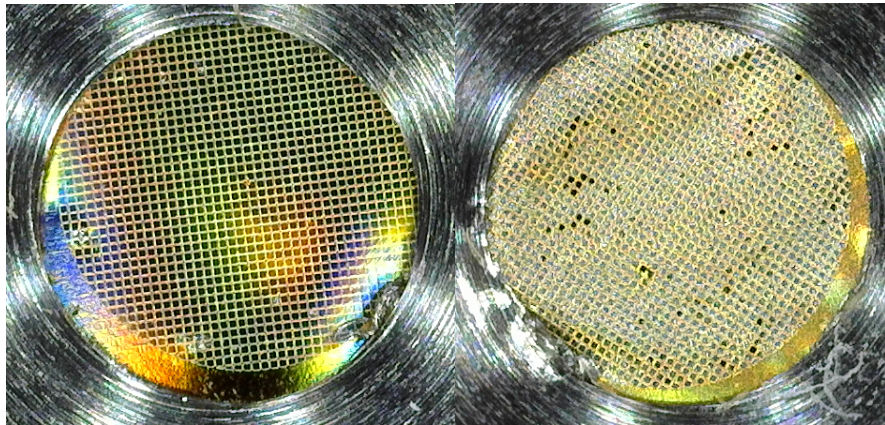
(a) Sketch of the SLG support

(b) Quantifoil with $1.2\ \mu\text{m}$ hole diameter

Figure 2.10: (a) Since the formvar cannot be fully dissolved after the carbon evaporation, a 20 nm Quantifoil consisting of 10 nm polyvinyl formal and 10 nm carbon layer on top remains. (b) For supporting the fragile single layer graphene a Quantifoil with $1.2\ \mu\text{m}$ hole diameter with a spacing of $1.3\ \mu\text{m}$ was chosen. Images taken from [57].

A detailed description of preparing clean graphene samples can be found in [58]. The commercial available graphene used for the following measurements was purchased by Graphenea. In general the Quantifoil-TEM grid is placed onto the chemical vapor deposition (CVD) graphene by using isopropyl alcohol for increasing the adhesion between the thin layer and the Quantifoil. After this the copper foil gets removed by placing the sample for 24 hours into ammonium persulphate, adding deionized water and subsequently lifting the TEM grid out of the solution. Typically 80-90% of the Quantifoil holes are covered with graphene.

For receiving EES from the support and compare it to the results of SLG, a TEM grid just covered by the Quantifoil without graphene on top was mounted in the target holder as well. This was essential to understand whether ions with high kinetic energies are able to traverse the Quantifoil support or are simply blocked by the latter, which is crucial for separating electrons emitted from the support from those originating from the graphene by means of coincidence measurements. In Section 4.1 this important question will be further elaborated. In Figure 2.11a a TEM grid covered by the Quantifoil support can be observed. In comparison to that Figure 2.11b shows the target of interest, i.e. the TEM grid with Quantifoil support covered by single layer graphene.



(a) TEM grid covered with Quantifoil support

(b) TEM grid and Quantifoil support covered with SLG

Figure 2.11: (a) The shimmering surface indicates the Au coating of a TEM grid with a Quantifoil support on top. (b) In addition to the Quantifoil layer the TEM grid is covered with single layer graphene. It is clearly visible that not 100 % are coated.

2.4.2 Thin carbon foils

Graphite is one of the most common allotropes of solid carbon, which also includes HOPG and graphene. In addition to these two cases it was decided to provide the target holder with extremely thin carbon foils to compare the EES results with those from SLG. For the preparation of such targets the given instructions in [59] were followed. The thin carbon foil (in a range between $1\mu\text{g}/\text{cm}^2$ and $20\mu\text{g}/\text{cm}^2$) mounted on a glass substrate was removed from the support by immersing it into water. The floating thin foil was captured by either a TEM grid or a stainless steel aperture (1–3 mm diameter). This preparation procedure of the carbon foil targets can be seen in Figure 2.12.

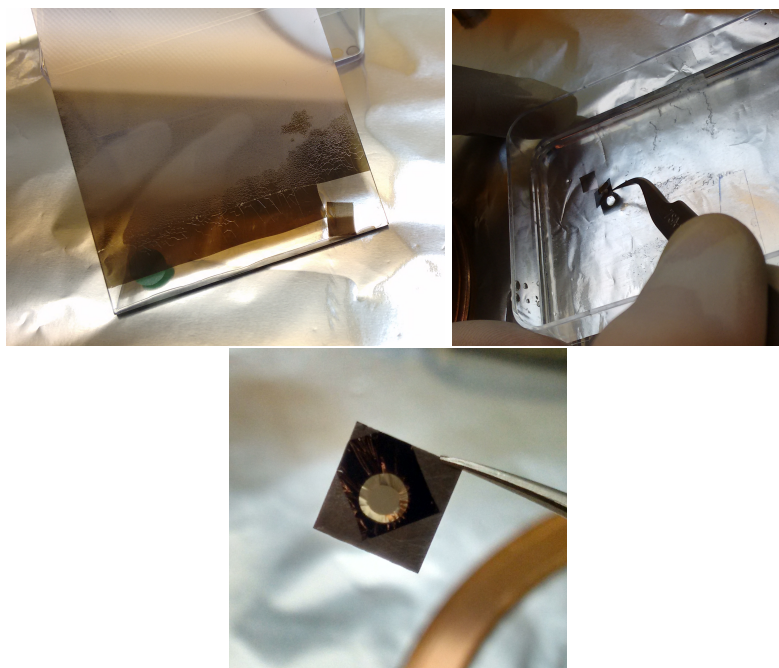


Figure 2.12: After cutting off a part of the carbon foil on the glass substrate it gets removed from the substrate by immersing it into water. The floating piece of carbon foil can now be captured by a TEM grid or an aperture.

According to [59] a bulk density of $2.00\text{ g}/\text{cm}^3$ is assumed and therefore, to achieve the equivalent thickness in nanometers, the areal density in $\mu\text{g}/\text{cm}^2$ has to be multiplied by 5.

For comparing the electron yield of single layer graphene resulting from the coincidence measurements performed, the target holder was provided with two similar carbon foils of $5\mu\text{g}/\text{cm}^2$ areal density mounted on a Au TEM grid and the other one on a stainless steel aperture with 1 mm diameter. Both targets already positioned in the slots of the target holder can be seen in Figure 2.13.

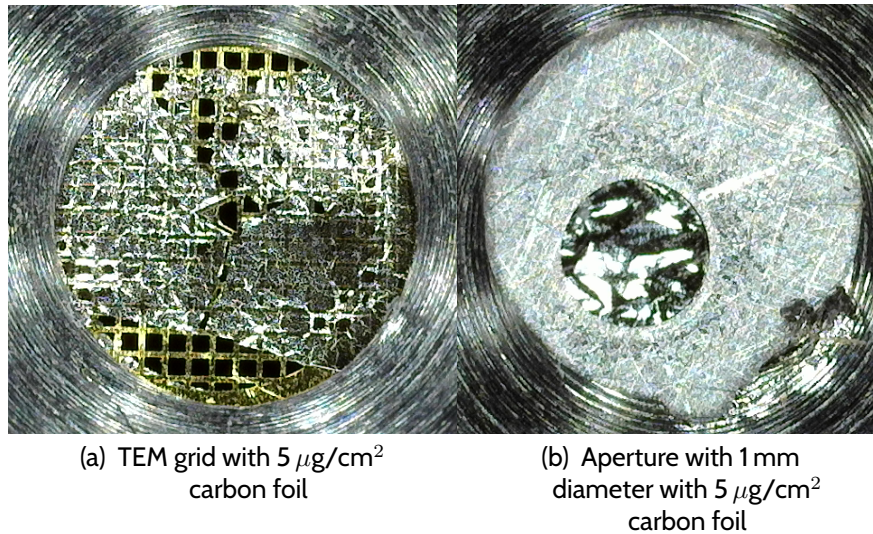


Figure 2.13: (a) The carbon foil target with the beam-exposed side facing up mounted on a not fully covered Au TEM grid. (b) The carbon foil covers the whole 1 mm aperture.

To check whether projectiles are able to penetrate through the $5 \mu\text{g}/\text{cm}^2$ carbon sample especially in the case of high impact energies, as a first attempt coincident spectra of these carbon targets were recorded. The nominally – according to [59] – 25 nm thick carbon foil fully covering the aperture (see Figure 2.13b) was bombarded with Ar^{9+} ions in the energy range 9–54 keV. The count rate received at the MCP detector was compared to the one obtained by removing the target holder from the ion beam. With the C-target inserted the count rate dropped to less than 2% of the value without C-foil, indicating that the used carbon foils are able to stop even 54 keV Ar^{9+} ions. Consequently only non-coincidence measurements were performed for the C-sample mounted on the aperture (cf. Figure 2.13b).

Despite the experimental observations numerical simulations with SDTRIM.SP (Static and Dynamic TRIM Sequential and Parallel software) for calculating the stopped fraction per penetration depth in amorphous carbon were performed for Ar projectiles. Based on Monte Carlo algorithm the transport of ions through matter is simulated, assuming a binary collision approximation (BCA) for the atomic collisions in an amorphous target [60–62]. Without any concerns a thickness of 25 nm should be sufficiently thick to stop 12 keV Ar ions (cf. Figure 2.14). This projectile impact energy was chosen for most of the performed measurements. Although no coincidences were experimentally received for 54 keV Ar ions impinging on the carbon sample (less than 2% of the value without C-foil), the fraction of these projectiles stopped by the carbon foil – according to the simulations (cf. Figure 2.14) – is almost negligible. This

discrepancy in experimental and numerical evaluation may be an interplay of different causes. One possible explanation could be that the actual thickness of the applied $5 \mu\text{g}/\text{cm}^2$ carbon foil is greater than the assumed 25 nm. In case of 80 nm carbon almost every projectile in the assumed energy range would be stopped by the sample, according to the SDTRIM.SP simulations presented in Figure 2.14. Multiple collisions and associated scattering processes of the projectiles within the target bulk, which will cause a deviation of the ions on their way through the sample, have to be considered as well. In this case most projectiles will no longer reach the MCP detector, which will reduce the chance for coincidences. Moreover, the actual stopping power within the first layers of the carbon target could be much higher than the one used in the simulations, leading to neutral projectiles, exiting the C-foil with very low velocity and therefore very low efficiency of being registered by the MCP detector.

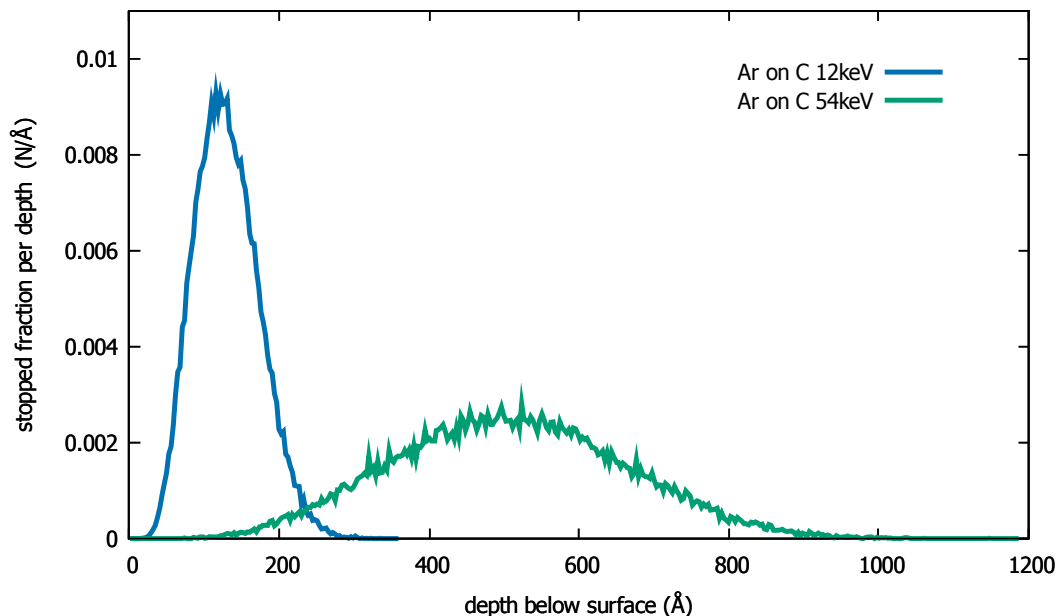


Figure 2.14: SDTRIM.SP simulation (performed by Bernhard Berger) presenting the stopped fraction per depth for argon impinging on carbon.

For the C-foil on the TEM grid (sample shown in Figure 2.13a) 20-30% of the incoming ions pass through holes and cause a signal at the MCP detector. Although in principle this would allow coincidence measurements for this carbon sample, no corresponding electron is emitted for ions traversing a hole. All coincidences measured are therefore random coincidences. They occur if another ion induces electron emission from the carbon foil within the still opened gate window caused by a previous projectile. For non-coincidence measurements from the C-foil mounted on the TEM grid, the resulting electron emission will be falsified by the contribution of electrons

emitted from the gold TEM grid (cf. Figure 2.13a).

Therefore all following results for amorphous carbon foils included in the present work were obtained by evaluating the electron emission yield for non-coincidence spectra from the C-foil mounted on the aperture (sample shown in Figure 2.13b). The impinging ion beam was adjusted precisely to ensure that no electrons were emitted from the surrounding support of the C-foil.

2.5 Electronics and data acquisition

The following section should give a short overview of the electronics used for data acquisition in this work. Figure 2.15 illustrates the main components essential for performing coincidence measurements.

In order to supply the PIPS detector with high voltage (29 kV) the whole setup for registering the emitted electrons is arranged in a faraday cage. An insulator separates the high voltage from the ground potential. When an electron impinges on the active area of the PIPS detector the thereby created electron-hole pair are captured by the bias voltage which leads to a charge-pulse at the detector output. This signal is extracted from the detector by a preamplifier (ORTEC 142B) without significantly degrading the signal-to-noise ratio. The preamplifier prepares the signal for the further processing in a shaping amplifier by means of integrating the received signal on a feedback capacitor resulting in a pulse proportional to the created charge in the semiconductor material. The output signal is amplified by a spectroscopy amplifier (ORTEC 570) and delayed by a subsequent delay amplifier (ORTEC 427A). Due to its pulse-shaping feature the former is essential for an accurate analog output signal (0–10 V) representing the deposited energy in the active area of the detector. The latter just delays the arriving pulse which becomes crucial for the performed coincidence measurements considering the much faster electrons compared to the heavier ion projectiles (cf. Section 2.6.2).

The resulting well-shaped and amplified signal is then pulse height analyzed and arranged into a histogram by a multichannel analyzer (MCA). The one used in this setup is provided by CAEN (Mod. N957). Via an optical USB cable the prepared spectrum of pulse heights versus number of electrons can be linked to the measurement computer on ground potential.

For reasonable coincidence measurements a gate signal is indispensable. The cascade of secondary electrons created in the microchannel plate detector by ions traversing the target, serves as such a signal. Once extracted from the anode, it gets preamplified (ORTEC 142A) and shaped in another amplifier (ORTEC 474). To gain accurate timing information from analog signals with varying heights but same rise time the signal is transformed into a constant fraction discriminator (ORTEC 437A). Guiding

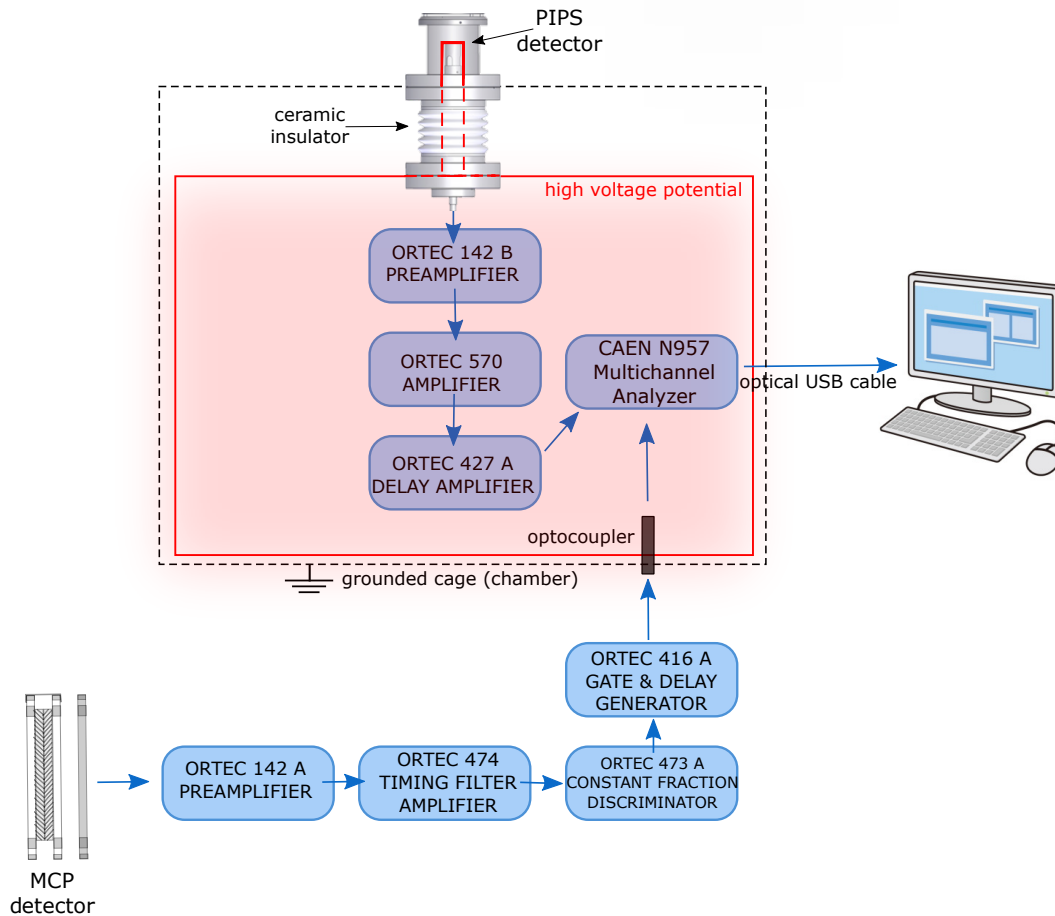


Figure 2.15: Schematic of the electronics used in the performed coincidence measurements.

the signal into a gate and delay generator (ORTEC 416A) provides the required gate pulse for feeding the external gate input of the MCA with a suitable signal. In order to transfer it to the multichannel analyzer at high voltage potential an optocoupler was used.

2.6 Coincidence measurements

Many investigations on ion-induced electron emission from metal (eg. clean gold [35] or polycrystalline aluminium [63]) and insulating surfaces (eg. polycrystalline lithium fluoride [21, 22]) as well as in coincidence with scattered projectiles in grazing incidence interactions [20] have been performed during the last two decades. In order to bridge the gap between collisions in solid and those in gaseous targets the use of

SLG samples became of major interest in this work. Thus studying electron emission phenomena in ion-surface interactions based on the electron emission statistics is a well-established technique [18] and the main task turned out to be the implementation of an ion detecting system enabling registration of both particle species at the same time.

2.6.1 Ion signal creating the gate

After extraction from the ion source the particle beam is focused onto the entrance of the sector magnet where a certain ion species with a specific mass over charge state ratio m/q is selected (cf. Figure 2.4). The kinetic energy E_{kin} of the resulting ion beam is defined by the chosen charge state q multiplied by the adjusted extraction voltage U . To investigate the electron emission yield in this work only noble gas Ar^{q+} ions with an atomic mass of $m = 39.948$ atomic mass units (amu) were applied. The kinetic energy that the ions gain by the extraction voltage will lead to an ion velocity v_i with which the projectiles will traverse the target and impinge on the MCP detector.

$$\frac{mv_i^2}{2} = qU \quad \rightarrow \quad v_i = \sqrt{\frac{2qU}{m}}. \quad (2.3)$$

The ion impact at the MCP detector causes a signal serving as a gate for the performed coincidence measurements. A detailed report on the gate creation and its following processing in the multichannel analyzer can be found in the master thesis of A.Fuchs-Fuchs [64].

2.6.2 Delayed electron signal

Comparing v_i with the velocity v_e that the emitted electrons gain by acceleration from the target surface to the high voltage potential applied at the PIPS detector will emphasize the need of delaying the much faster electron signal. Due to their smaller mass ($m_e = 5.489 \cdot 10^{-4}$ amu) the electrons will reach the detector within a much shorter time than the corresponding ion signal will be registered by the MCP. The required delay time t that has to be applied to the measuring system to obtain true coincidences was investigated in detail in [64] and found to be between 0.29 and 2.16 μs depending on the ion charge state and the applied extraction voltage.

2.7 Measuring procedure

2.7.1 Determination of the operating point

For achieving the highest electron collection efficiency the influence of different potentials in the target chamber on the emitted electrons has to be taken into account. The end-aperture as well as the sample holder are grounded but biasing both electron repeller and the highly transparent grid plays a crucial role for focusing the electrons of interest onto the active area of the PIPS detector. For optimizing the collection efficiency numerical simulations for the electron trajectories for similar geometries were performed in the past [52]. Thus, a rough first guess of the necessary voltages at the collection grid and the electron repeller became possible.

Nevertheless, due to particular changes to the setup, a series of yield optimizing measurements with varying grid and repeller potential had to be executed to obtain the ideal operating point with collection efficiencies close to 100 %. A detailed description of this experimental procedure and accompanying 3D-simulations for the resulting electron trajectories in the actual geometry of our new setup can be found in [64]. The ideal operating point for the performed measurements under an impact angle of $\vartheta=45^\circ$ was found in applying a positive grid potential of 210 V and biasing the electron repeller with -500 V.

2.7.2 Settings for coincidence measurements

After testing the electron detection branch with an auto-gate mode integrated in the MCA, which totally neglects the ion signal arising in the MCP detector, gate settings had to be found for performing coincidence measurements for the target of interest. As mentioned above the ions traversing the single layer graphene target reach the detector much later than the corresponding electrons and so delaying the electron signal becomes inevitable. Before every coincidence measurement the necessary delay time is calculated for the appropriate ion charge state and kinetic energy and is adjusted to the measurement system.

The applied gate and delay generator offers the opportunity of varying the gate width in a range between $0.4\mu\text{s}$ and $4\mu\text{s}$. According to [65] for operating in the external gate mode the incoming gate signal must occur prior to, and must extend for at least $0.2\mu\text{s}$ after the peak. Adapted to the received electron signal pulse shape in this case a suitable gate width of $2\mu\text{s}$ was selected. For further details on the optimizing of the required gate settings once again [64] can be consulted.

A crucial role plays also the avoidance of receiving pileups. If the incoming ion current is too high a superposition of several electron events can occur. One opened gate covers this overlapping pulse, which leads to a very noisy and falsified spectrum. Therefore, multiple projectile hits of the surface within the gate width of $2\mu\text{s}$ have to be avoided by keeping the impinging ion rate as low as possible (in any case less than 10 kHz). By leading the gate signal, as well as the ion-induced electron pulses into an oscilloscope before processing in the MCA, the permanent monitoring of this disturbing pileups becomes possible. The impinging ion current at the end-aperture is always recorded and, by varying the applied voltages at the deflection plates as well as those at the einzel lens, pileups in the electron signal can be easily reduced to an acceptable level.

2.7.3 Calibration

The MCA sorts the received electron signal into a histogram with 8192 channels. For allocating each peak in the resulting spectrum to a number n of simultaneously emitted electrons a calibration has to be executed before starting a measurement. The energy of the electrons deposited in the PIPS detector is directly proportional to the applied voltage. By recording spectra at different acceleration voltages applied to the PIPS detector and adjusting the MCA channels to the corresponding number of electrons a reliable calibration can be achieved. Figure 2.16 exemplifies the performed calibration process, in which the received peaks were assigned to the suitable number of emitted electrons at four different PIPS voltages. The slope for the detected peaks increases with increasing applied voltage, the crossing point of their fit functions indicates the case in which no electron was emitted from the target surface. This calibration procedure is essential, since in some occasions the first peak of a spectrum is masked by a strong peak resulting from the intrinsic noise of the detector. The calibration method described allows to correct for such an uncertainty, ensuring that the first peak visible in each spectrum indeed corresponds to the one electron peak.

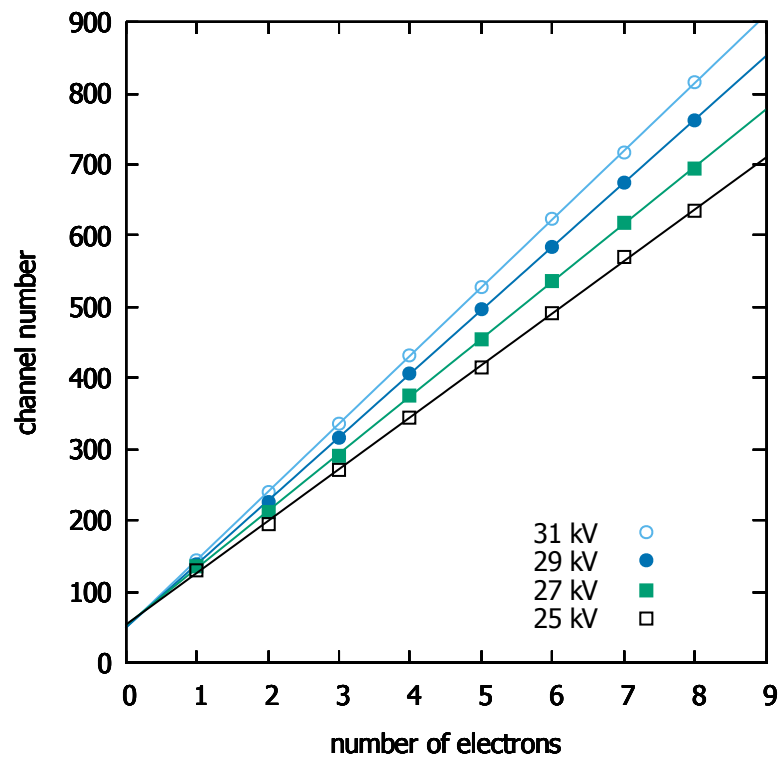


Figure 2.16: For matching the MCA channels to the corresponding number of emitted electrons a calibration has to be performed at different acceleration voltages. The slope of the fit function increases with increasing voltage but all fit functions cross at a single point, which indicates the fictional case for zero electron emission.

3 Evaluation concept

3.1 Electron emission statistics

A well-established technique for detecting electrons originating from ion-surface interaction processes is by means of electron number statistics. A positively biased energy sensitive PIPS detector extracts the ion-induced electrons emitted from the surface, allowing to determine the number of emitted electrons at every projectile impact. PE processes expire within 10^{-13} s [15], while subsequent KE events last no longer than 10^{-12} – 10^{-11} s [66]. With a time resolution of about $0.5 \mu\text{s}$ of the detector electronics all emitted electrons induced by one projectile will reach the active area of the PIPS detector within this time window, and will therefore be counted in one pulse. Consequently the number of emitted electrons per ion can be deduced from the pulse height distribution of the detector. The great advantage of this method, compared to other yield evaluation techniques, is well-founded in receiving the statistics of electron emission, and not exclusively their average number. Such a statistics plays a crucial role when it comes to registration of extremely small particle currents, which is no longer feasible with conventional measurement methods. It reveals the probabilities W_n for the simultaneous emission of n electrons resulting from a single ion impact event. Hence, the total electron yield γ can be derived as the mean value weighted with the individual probabilities

$$\gamma \equiv \bar{n} = \sum_{n=1}^{\infty} nW_n, \quad \sum_{n=0}^{\infty} W_n = 1. \quad (3.1)$$

For n independently emitted electrons it is commonly assumed that the EES obeys a binomial distribution, which leads for a large ensemble of emitted electrons in to a Poisson distribution $P_n(\gamma)$

$$P_n(\gamma) = \frac{\gamma^n}{n!} e^{-\gamma}. \quad (3.2)$$

The counting loss, i.e. the probability W_0 of no electron emission, can then be estimated by fitting a Poisson distribution to the measured EES

$$W_0 \approx P_0 = e^{-\gamma}. \quad (3.3)$$

At small electron yields, i.e. $\gamma \simeq 2$, the counting loss can no longer be neglected.

Various groups have investigated the deviation of a measured EES from a Poisson distribution. In the case of small total electron yield, and especially for PE processes, the electron emission statistics clearly shows no longer a Poissonian behaviour. Furthermore Delaney and Walton [?] attributes a deterioration of the received spectra to electron backscattering from the PIPS detector surface, which has to be strongly taken into account while evaluating EES. If n electrons originating from an ion impact event impinge on the detector surface there exists a non-negligible probability for 0,1,2... up to n electrons being backscattered from the surface. These reflected electrons will only deposit a fraction of their original energy, leading to a characteristically structured background between the individual peaks. Asselt *et al.*[67] investigated the electron emission spectra more precisely by taking into account the effect of such backscattered electrons.

Considering the possibility of backscattered electrons from the applied PIPS detector surface in [17] and [18] one of the first correct interpretations of EES were introduced. The authors presented an evaluation concept, in which the contribution of backscattered electrons was included quantitatively. For particles impinging on the PIPS detector with 30 keV the probability for backscattering can be assumed to be $p_{Si}=17\%$ for silicon and $p_{Al} \approx 15\%$ for aluminum covering the silicon active area of a PIPS detector. A Gaussian energy distribution with mean energy and full width at half maximum (FWHM) of 60% and $\sim 40\%$ of their original energy E_e is assumed for the reflected electrons, respectively [17, 18].

The authors in [17] and [18] fitted their measured EES spectrum $S(E)$ to a linear combination of normalized functions $F_n(E)$, which correspond to the respective emission events of n ejected electrons per incident ion projectile

$$S(E) = \sum_{n=0}^{n_{\max}} C_n F_n(E), \quad (3.4)$$

where C_n represent fitting parameters related to the peak area of the n th contribution, and therefore also to the emission probabilities $W_n = kC_n$, where k indicates only a constant value. Without electron backscattering these functions $F_n(E)$ would obey a Gaussian distribution centered around $n \cdot E_e$. Including the possibility for reflection of $m = 0, 1, 2, \dots, n$ electrons from the detector surface each $F_n(E)$ can be determined as a sum of individual peaks $f_n(E, E_m, \Delta E_m)$ correlated to m backscattered electrons

$$F_n(E) = \sum_{m=0}^n P_n(m) f_n(E, E_m, \Delta E_m). \quad (3.5)$$

$P_n(m)$ states the probability for backscattering of m out of n electrons arriving at the detector and obeys the binominal statistics

$$P_n(m) = \binom{n}{m} p^m (1-p)^{n-m}, \quad (3.6)$$

where p represents the backscattering probability for a single electron mentioned above.

The $f_n(E, E_m, \Delta E_m)$ themselves are normalized, Gaussian-shaped functions, centred around

$$E_m = n \cdot E_e - m \cdot 0.6 \cdot E_e \quad (3.7)$$

with a FWHM

$$\Delta E_m = \sqrt{(\Delta E_{\text{Det}})^2 + m(\Delta E)^2}, \quad (3.8)$$

where ΔE_{Det} and ΔE represent the energy resolution of the detector and the FWHM of the main peak, respectively.

Figure 3.1 presents as an example the contributions of $m = 0..4$ backscattered electrons to the function $F_4(E)$ in the case of $n = 4$ simultaneously arriving electrons at the detector surface.

By fitting the electron emission statistics to the observed spectra, the fitting parameters C_n – and consequently the emission probabilities W_n – can be deduced, allowing to compute the total electron emission yield γ according to Equation 3.1.

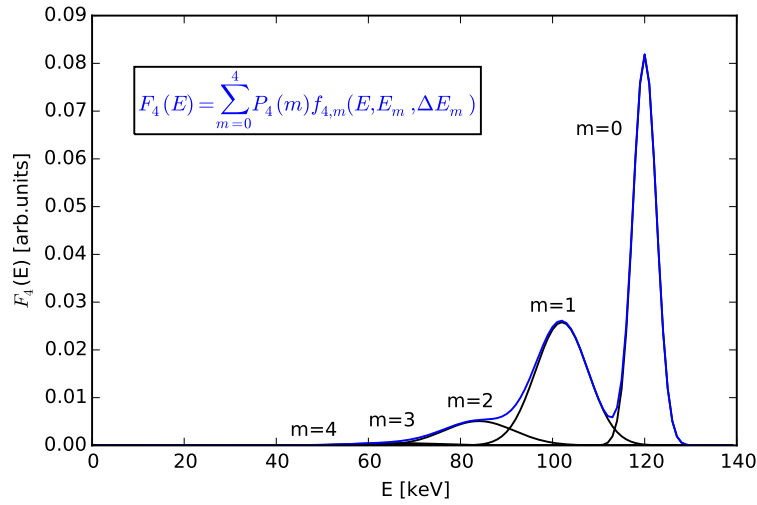


Figure 3.1: Simulated pulse height distribution for $n = 4$ simultaneously impinging electrons onto the PIPS detector with an impact energy of 30 keV. The black curves represent the individual normalized Gauss functions for $m = 0 \dots 4$ backscattered electrons, whereas the blue line indicates the resulting function $F_4(E)$. A probability for backscattering of 15% was assumed. For the reflected electrons a Gaussian energy distribution was supposed with a mean energy at 60% and a FWHM of about 40% of their original energy.

3.2 Yield calculation for received EES spectra

In his diploma thesis M. Simon [29] presented an evaluation procedure for EES with high electron emission yield ($\gamma > 20$). In these spectra electron backscattering makes the identification of individual peaks nearly impossible and leads to an almost Gaussian-shaped pulse height distribution. The method he used is therefore based on determining the mean value of this Gaussian peak γ_{Gaussian} and linking it to the average yield. The center of the Gaussian is by an easily distinguishable factor α lower than the actual electron yield due to the electron backscattering. This correction factor α can be applied to the evaluation of every EES spectrum, its elaborated calculation can be found in [29].

$$\gamma = \alpha \cdot \gamma_{\text{Gaussian}}, \quad \alpha = \frac{1}{1 - p(1 - d)}, \quad (3.9)$$

where p corresponds to the probability for backscattering, and d to the average energy deposited by backscattered electrons. The implementation of a χ^2 -Fit-Fortran

routine did not deliver satisfying results and thus a visual fit procedure FitVisual.xls in Microsoft Excel was presented in [29]. The correction factor α as well as the individual probabilities W_n for n emitted electrons could be extracted, allowing the determination of the total electron emission yield γ .

In the beginning of the present work FitVisual.xls was considered for evaluating the yield from the performed measurements. However, the implementation of a Python routine for automated spectra fitting and yield evaluation was necessary. Especially due to lower yields ($\gamma < 20$), the method of fitting an appropriate Gaussian and linking the centre of the Gaussian to the average yield seemed not to be the appropriate choice for analyzing the electron emission spectra from single layer graphene.

The Python routine used to compute the final results was first introduced by Alexander Fuchs-Fuchs in his diploma thesis [64] and elaborated in the present work with the indispensable support of Lukas Rachbauer during his bachelor thesis [68]. Except from determining the total electron emission yield γ by means of EES, the implemented program also focuses on the rejection of the intrinsic detector noise as well as properly accounting of background contributions. Both is essential when it comes to the interpretation of low-yield emission spectra.

The evaluation procedure will be shortly presented here, for a deeper insight the bachelor thesis of L. Rachbauer [68] is strongly recommended and can serve as a manual for the Python script *calcyield3*.

After an appropriate calibration procedure as presented in Section 2.7.3 the position of the first peak corresponding to the emission of one electron for a certain applied acceleration voltage can be deduced. Figure 3.2 illustrates that this one electron peak usually resides on the shoulder of a huge, almost perfectly Gaussian-shaped, intrinsic detector noise peak. To reveal the requested electron peak a Gaussian was fitted to the noise peak, and subtracted from the rest of the data.

In addition to the coarse calibration accomplished by varying the acceleration voltage at the PIPS detector, and allowing estimation of the assignment of the channel number to the corresponding electron number, each measured spectrum can be individually calibrated by the applied Python routine. For such a purpose a special peak detection algorithm is implemented, which enables finding a peak by a characteristic shape instead of using its height [68]. With such an algorithm, also peaks covered by noise can be located. The received peak position i is assigned to the suitable number of emitted electrons n by means of a linear fitting curve with an adequate slope k and offset d , as

$$i = k \cdot n + d. \quad (3.10)$$

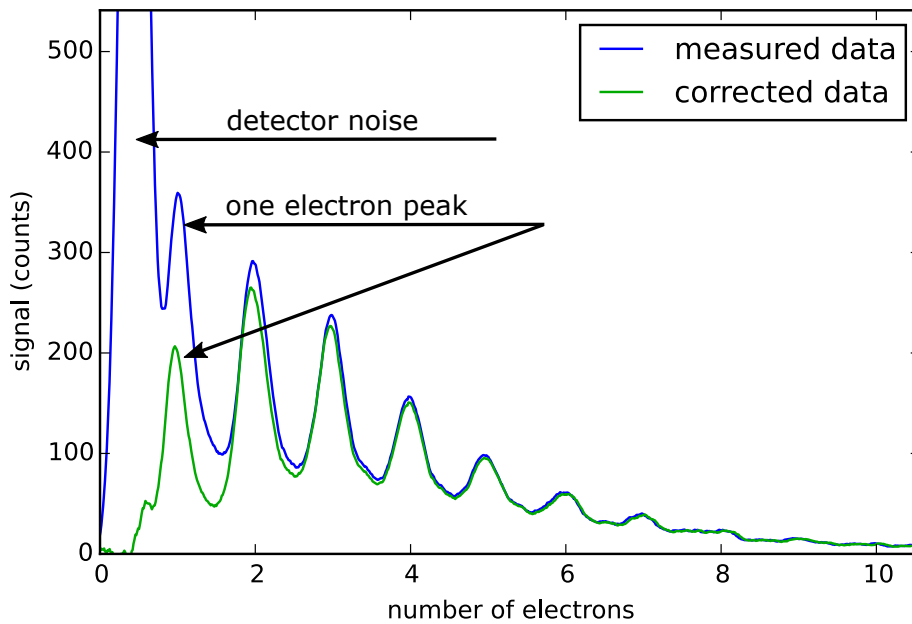


Figure 3.2: The peak representing the emission of one electron is overlapping with the Gaussian-shaped detector noise peak, which has to be subtracted from the data. The blue line indicates the measured spectra recorded by the PIPS detector, while the green line represents the already corrected data by subtracting the detector noise peak as well as the background.

Figure 3.3 depicts an example of such a calibration, in which the channels are matched to the number of emitted electrons.

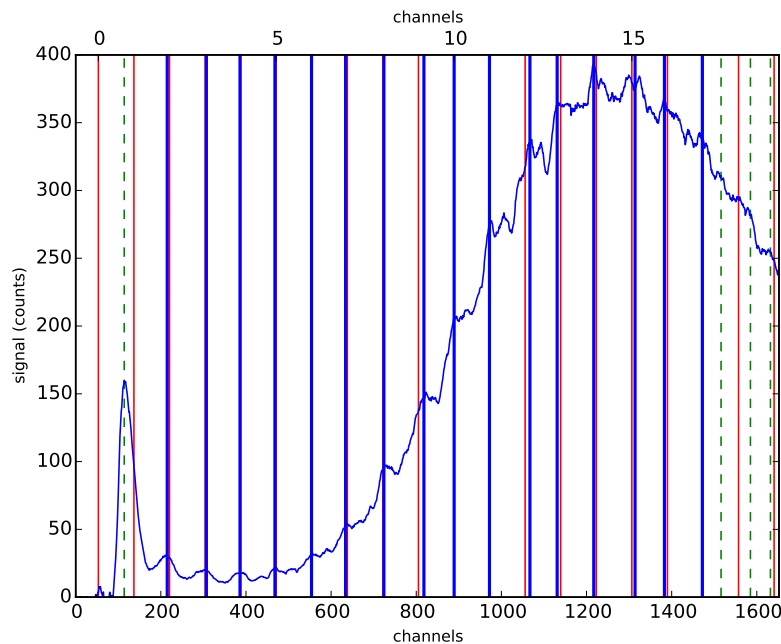


Figure 3.3: The detected peaks are separated in those which are not taken into account for further yield calculations, and therefore are rejected (green dashed lines), and those which are accepted by the Python routine (blue lines). The performed calibration results in the assignment of channels to the corresponding number of emitted electrons (red lines) [68].

Even in cases when no sample is exposed to the ion beam in the experimental chamber, a pulse height distribution can be registered at the PIPS detector. This background spectrum originates from several effects. On the one hand, there is a chance for field emission (e.g. from the collection grid positioned in front of the detector) which results in a very high one-electron emission peak. On the other hand the ions can impinge on the walls of the experimental chamber from where electrons can be collected with low collection efficiency. Both effects lead to a low-yield electron emission spectrum. Especially in case where the actual spectrum also shows a low yield difficulties arise in the EES evaluation and a careful treatment of the background becomes essential.

For each applied ion species with a certain kinetic energy a background pulse height distribution was recorded. First the intrinsic detector noise is eliminated as described above. Then the background spectrum as well as the one originating from ion collisions with the sample is calibrated by the implemented Python routine. After matching the calibrated electron-number axes of the background and raw data by proper rescaling, the former spurious contributions can be subtracted, resulting in EES contri-

butions arising exclusively from ion impact. As an example the subtraction procedure for receiving the electron emission spectrum for bombardment of SLG with 12 keV Ar^{3+} ions is demonstrated in Figure 3.4.

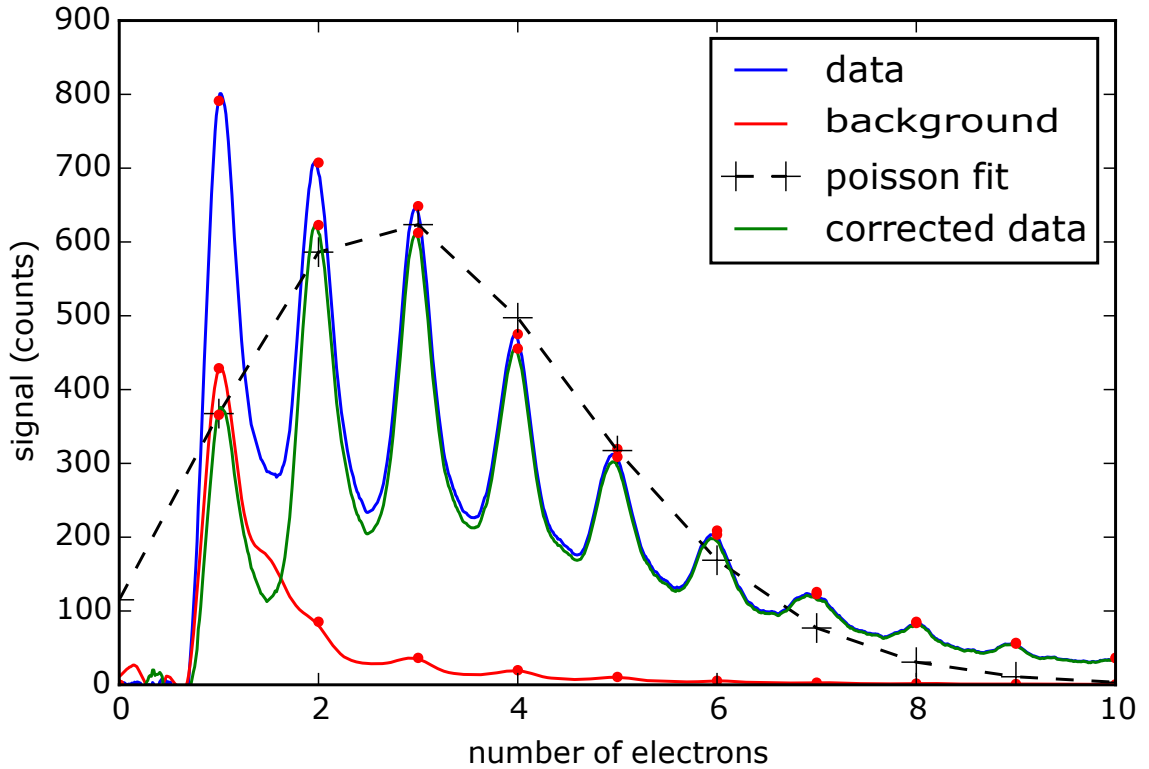


Figure 3.4: After matching the calibration (peak positions) of the background (background) to the one of the target spectrum (data) the actual requested pulse height distribution (corrected data) arises from a subtraction (data minus background).

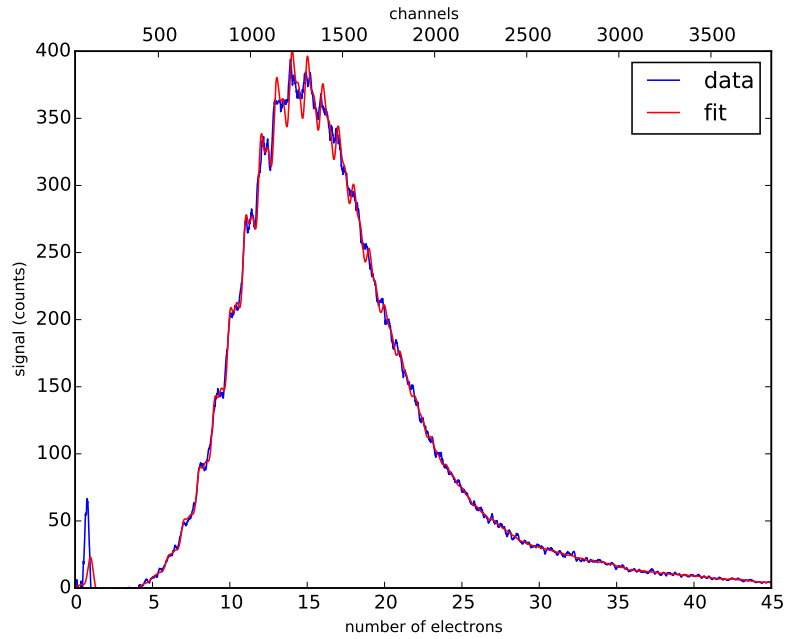
The total electron emission yield γ from the corrected data can now be achieved by means of EES (Equation 3.1). By

$$W_n = \frac{C_n}{\sum_{n=0}^N C_n}, \quad \sum_{n=0}^N W_n = 1, \quad (3.11)$$

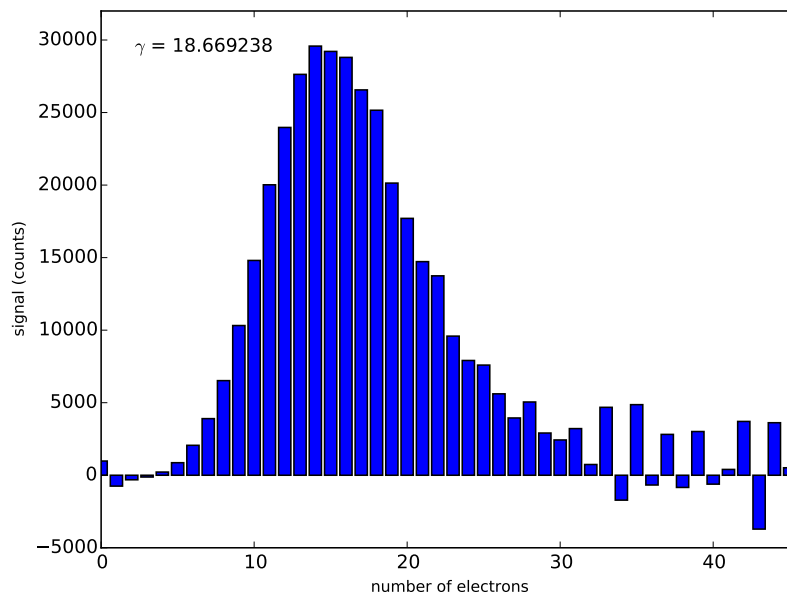
the required probability for the emission of n electrons per projectile is determined. Therefore the fitting of the spectrum to N normalized functions F_n , as it is indicated in Equation 3.4 and described in detail in Section 3.1, is required. By means of implementing a least squares optimization, the fitting parameters C_n are obtained. Instead

of reaching the minimization by varying the different C_n it turned out to be beneficial to assume a linear combination of a number of Poisson distributions for such fitting parameters, and determine the free Poisson parameters rather than the C_n [68]. Figures 3.5, 3.6 and 3.7 compare the different approaches. A least square fit of the C_n s gives unrealistically high fluctuations in the fitting parameters especially for high-yield spectra and even negative coefficients. Two Poissonian distributions behave much better (cf. Figure 3.6a, 3.6b), while in general three Poissonian are used for receiving results from spectra with $\gamma > 5$ (cf. Figure 3.7a,3.7b).

By determining the probabilities W_n for the emission of n electrons according to Equation 3.11, the total electron emission yield γ can be finally calculated in terms of Equation 3.1. Figure 3.8 presents the received results of the performed evaluation procedure for 54 keV Ar^{9+} ions impinging on single layer graphene under an incidence angle of 45° with respect to the surface normal. The individual emission probabilities W_n are plotted in Figure 3.8a, while Figure 3.8b reveals the contribution of the individual n -electron probabilities to the electron emission statistics. Assuming a linear combination of three Poisson distributions for the fitting parameters C_n an electron emission yield $\gamma=18.53$ was calculated for Ar^{9+} bombardment of SLG with a kinetic energy of 54 keV.

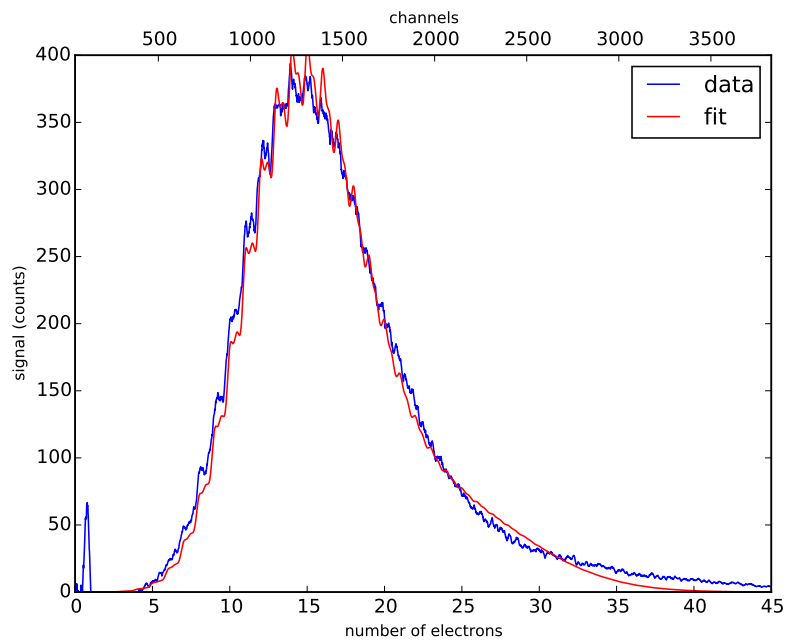


(a) Fit with directly determined fitting parameters C_n

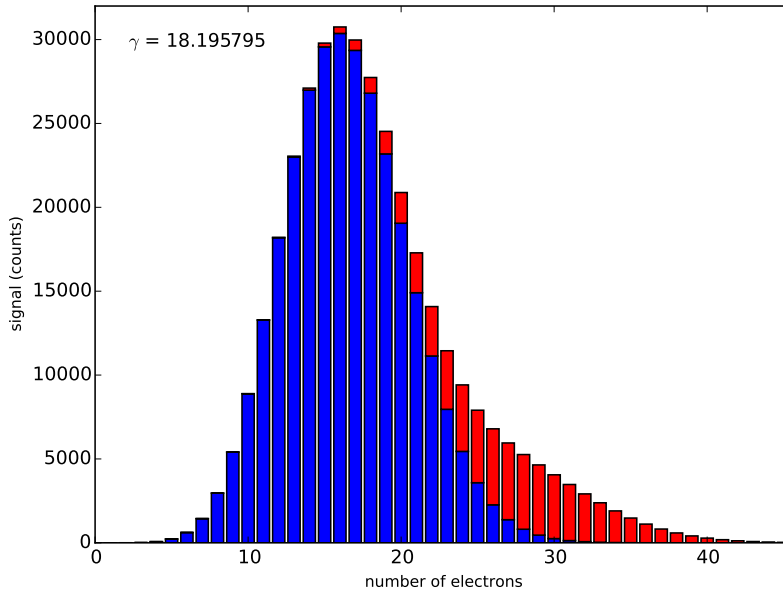


(b) C_n directly determined

Figure 3.5: Least squares optimization by varying the fitting parameters C_n . For a high number of emitted electrons the backscattering structure becomes dominant, and leads to unrealistic values for the C_n s, which are directly related to the emission probabilities. Figures taken from [68].

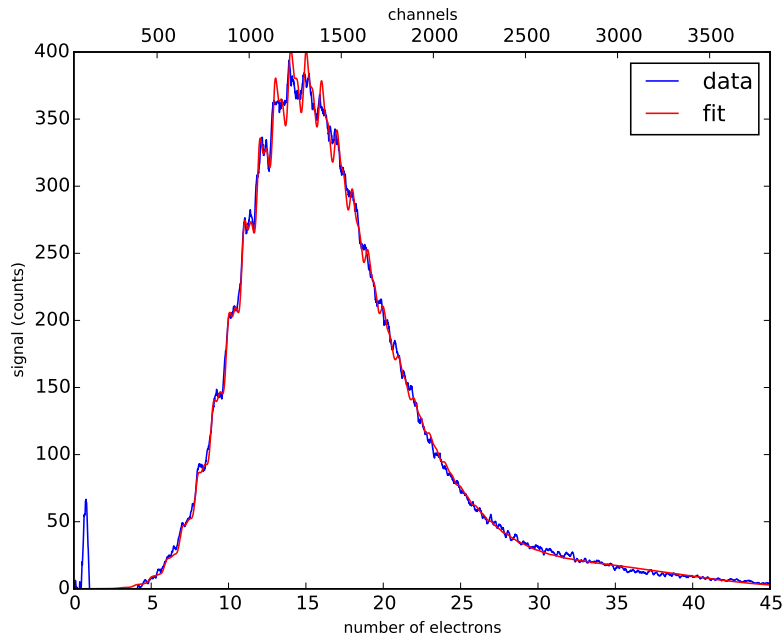


(a) Fit with C_n obtained by two Poissonian

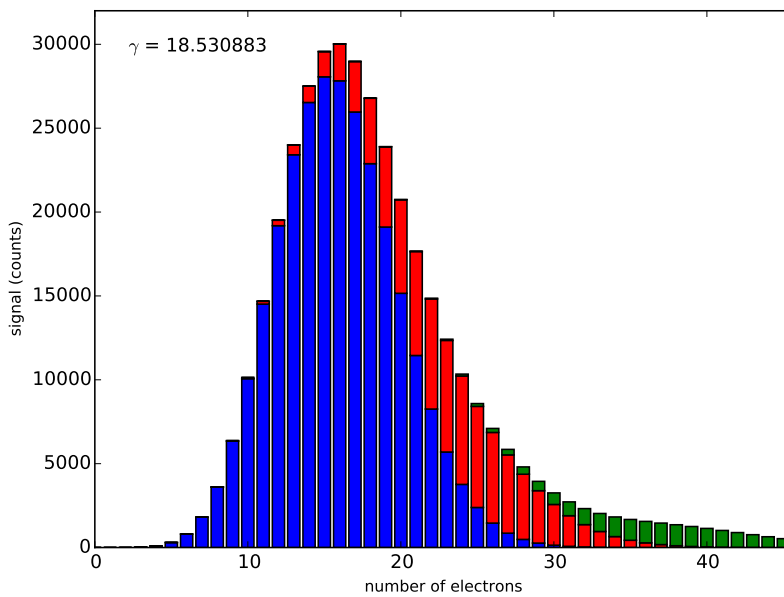


(b) C_n achieved by two Poisson distributions

Figure 3.6: Two Poisson distributions for the fitting parameters behave much better than using a least square fit for the C_n s. Figures taken from [68].

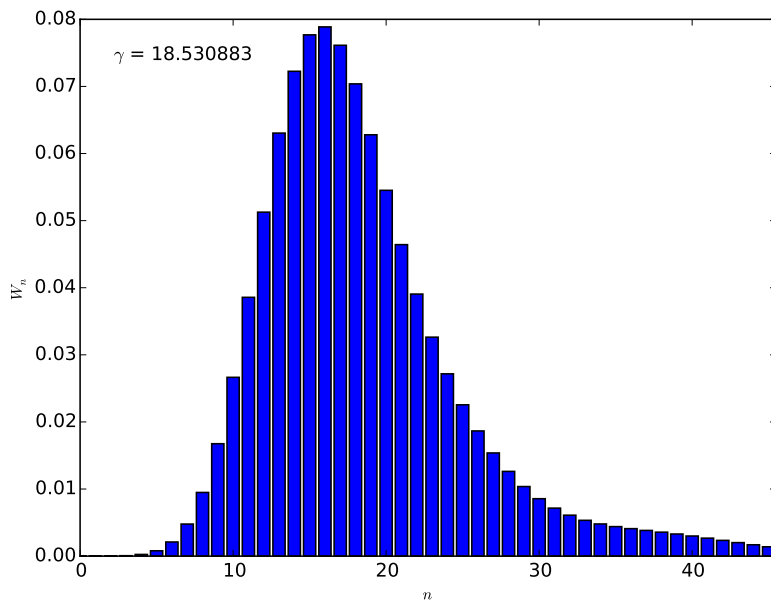


(a) Fit with C_n obtained by three Poissonian

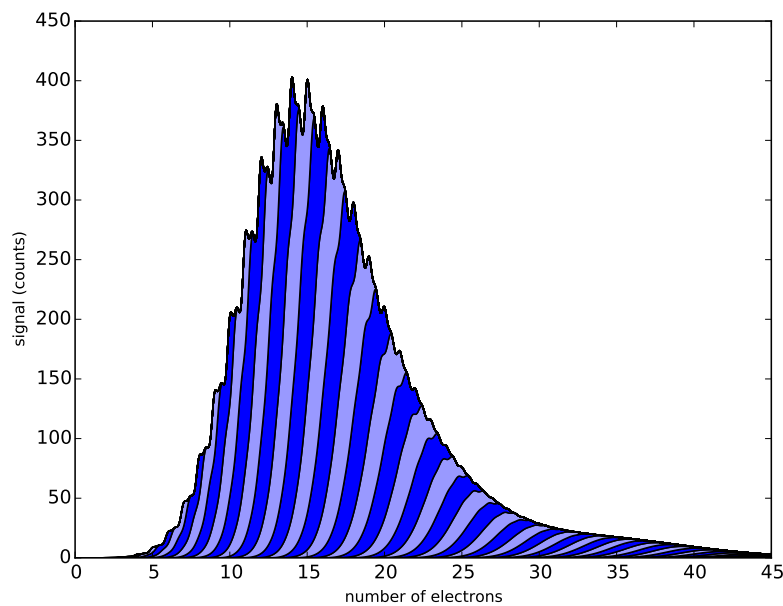


(b) C_n achieved by three Poisson distributions

Figure 3.7: Assuming a linear combination of three Poisson distributions for the fitting parameters is especially needed for electron emission spectra with high electron yield. Figures taken from [68].



(a) Probabilities for n emitted electrons



(b) Typical electron emission statistics, in which the contribution of each of the n emitted electrons is color-coded

Figure 3.8: EES for bombardment of SLG with 54 keV Ar^{9+} ions under an impact angle of 45° with respect to the surface plane.

4 Results & Discussion

4.1 Coincidence spectra in comparison to non-coincidence measurements

For receiving electron emission statistics from the desired SLG sample a properly controlled coincidence measurement method is necessary. Therefore, a primary focus in the present work was put on performing such coincidence measurements, and on comparing the later with the results obtained by non-coincidence spectra. Such a comparison aims at clarifying the paramount relevance of performing coincidence measurements in ion-induced electron emission from SLG. The data-processing multichannel analyzer allows to easily switch between external and auto gate modes. Coincidence measurements are performed in the external gate mode by recording the incoming electron signal only in the case of an opened gate window, caused by traversing ions impinging on the MCP detector (see Section 2.6 for details). The auto gate mode is instead applied for achieving non-coincidence spectra, which corresponds to recording all incoming electron events whether they are originating from the SLG target or from the underlying support.

To compare now the results for non-coincidence and coincidence spectra recorded for the single layer graphene target (cf. Figure 2.11b) the sample position was carefully optimized with the $xyz\varphi$ -manipulator in order to exactly hit the target with the adjusted ion beam. The arriving ion current was registered at the end-aperture (cf. Figure 2.5) before entering the experimental chamber, while the gate count rate was monitored by an oscilloscope. The coincident and non-coincidence pulse height distributions were recorded directly, one after the other without changing the target position. As an example Figure 4.1 presents two resulting spectra received by this procedure. Under an impact angle $\vartheta = 45^\circ$ with respect to the surface normal SLG was bombarded with 12 keV Ar^{5+} ions. In one case the emitted electrons were registered in coincidence with the traversing ions, while in the other case all emission events were recorded by the PIPS detector. The solid lines in Figure 4.1 show the obtained fitting curves while the dashed vertical lines present the total electron emission yield, calculated from the corresponding spectra following the evaluation process described in Section 3.2. For such broad distributions the calculated yield strongly deviates from the mean value of a corresponding Gaussian, but regarding the probability distributions W_n for n simultaneously emitted electrons (cf. Figure 4.2) confirms the yield

evaluation. Due to the much higher count rate in the case of not coincidence measurements apparently the two spectra differ from each other considering the absolute number of counts. Nevertheless, also a difference in their emission yields, $\gamma=9$ for the non-coincidence spectrum and $\gamma=8$ in case of coincident recording, can be deduced. Such a difference in the emission yield of at least one extra electron primarily arises from the support material in the EES of the SLG, qualifying coincidence measurements as more appropriate for such kind of samples.

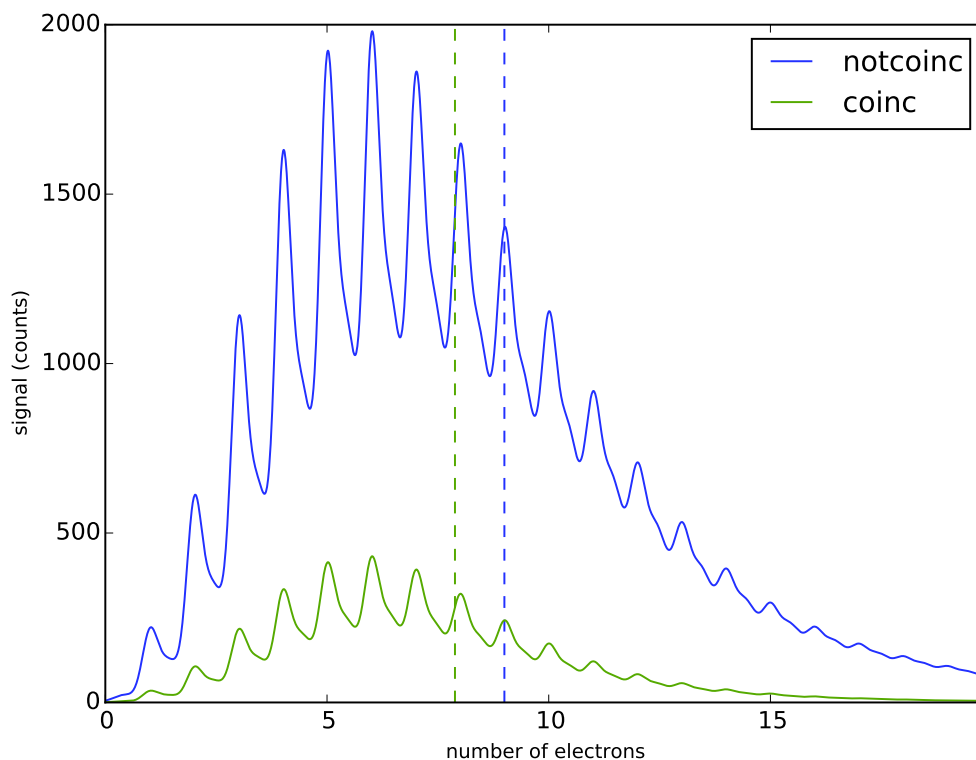
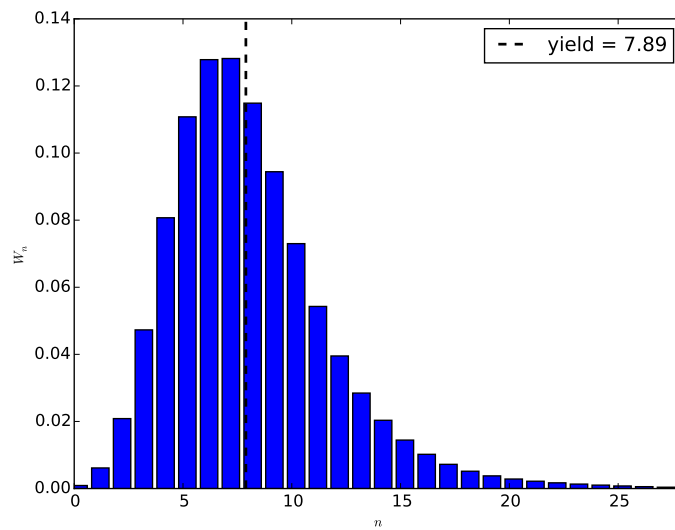
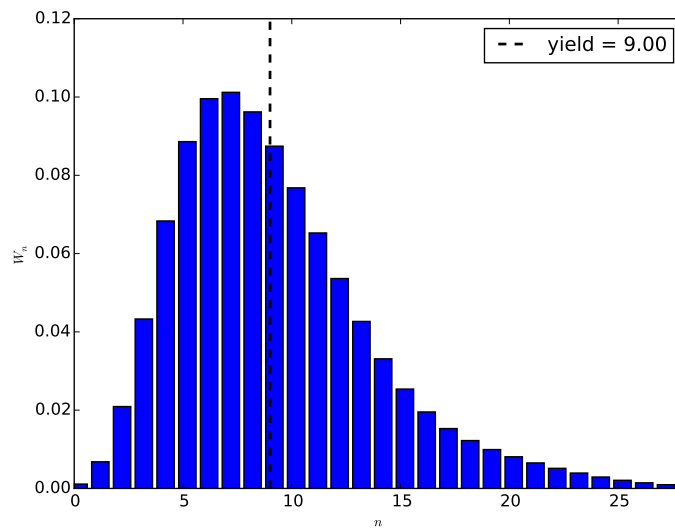


Figure 4.1: Measured spectra for SLG bombardment with 12 keV Ar^{5+} ions under an impact angle of 45° with respect to the incoming projectile beam. A coincident measurement by registering only electrons with a corresponding ion signal (green solid line) as well as a non-coincidence measurement recording all emission events (blue solid line) were performed. With $\gamma=8$ (green dashed line) for the coincident and $\gamma=9$ (blue dashed line) for the non-coincidence case a difference in the emission yield can be concluded.

In order to further demonstrate the differences in the results when performing coincident and non-coincidence measurements for single layer graphene mounted on



(a) EES for coincidence measurement



(b) EES obtained by non-coincidence recording

Figure 4.2: Probability distribution W_n for n simultaneously emitted electron induced by 12 keV Ar^{5+} impact on SLG. For both the coincident (a) and the non-coincidence (b) EES the obtained yield deviates strongly from the mean value of a corresponding Gaussian distribution, due to non-negligible contributions of high- n electron emission.

its support, a series of emission spectra were recorded. Figure 4.3 presents the outcome of such a series including EES data for different incident ion charge states. Once more an angle of $\vartheta=45^\circ$ with respect to the surface plane was chosen, and – by varying the extraction voltage at the ion source – the kinetic energy of the different charge state projectiles was set to 12 keV. At each selected charge state q the non-coincidence spectrum exhibits a slightly higher electron emission yield γ with respect to the coincident measurement, even though the results become more similar with increasing charge state.

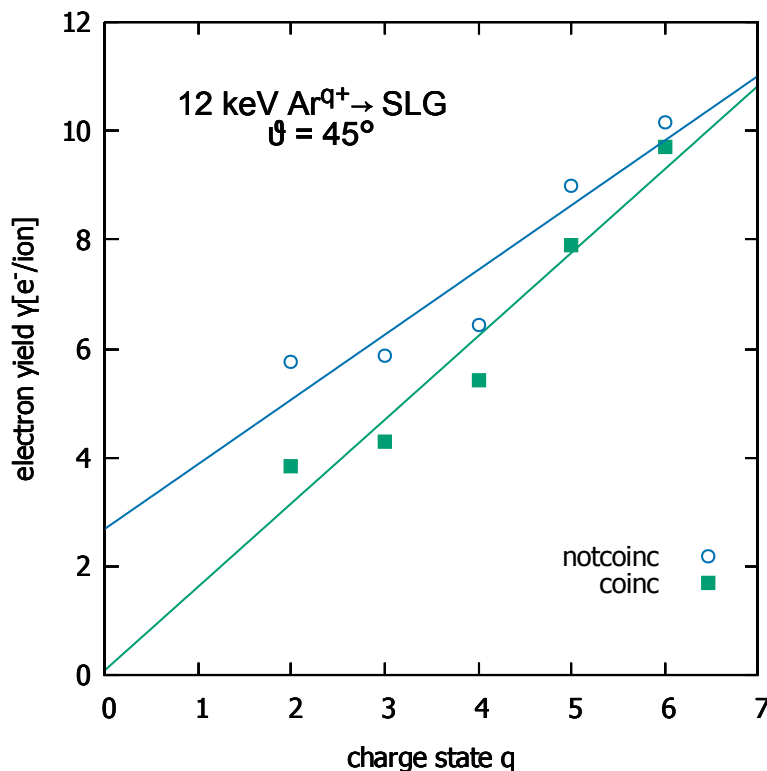


Figure 4.3: Charge state dependence of Ar^{q+} -induced electron emission yield for coincidence and non-coincidence EES from SLG. For all projectiles the incident energy was set to 12 keV and the impact angle to 45° . For every charge state the electron yield obtained by the coincident measurement is lower ($\approx 1e^-$) than the one calculated from the non-coincident spectrum.

Although there is a recognizable difference in the performed EES for SLG with and without its support the possibility for ions traversing the Quantifoil was conceivable. Coincident as well as non-coincidence spectra were recorded for the support material to enable later evaluation. If the Quantifoil is thick enough to stop a certain ion the received coincidence spectrum can be attributed to random coincidences. Therefore a method to ascertain, whether a pulse height distribution results from true co-

incidences or rather random ones, is to calculate the rate of possible random coincidences I_c^{rand} and compare it to the actually measured coincidence count rate I_c^{meas}

$$\frac{I_c^{\text{rand}}}{I_c^{\text{meas}}} \quad \text{with} \quad I_c^{\text{rand}} = W_i \cdot I_g. \quad (4.1)$$

I_c^{meas} amounts to the integrated number of coincidentally measured emission events for a single coincidence spectrum (e.g. area below the green curve in Figure 4.1), divided by the measurement time, while I_g represents the gate count rate registered at the MCP detector. W_i represents the calculated probability for an ion to reach the sample while the gate of the previous one is still opened. Considering a time τ between two extracted ions, W_i is determined by integrating the probability density function $dW_i(\tau)/d\tau$ within the time $\tau \in \{0, T\}$ in which the gate is opened

$$\begin{aligned} \frac{dW_i}{d\tau}(\tau) &= I_i \cdot e^{-I_i \cdot \tau}, \\ W_i(T) &= \int_0^T \frac{dW_i}{d\tau} d\tau, \\ W_i(T) &= 1 - e^{-I_i \cdot T}, \end{aligned} \quad (4.2)$$

where I_i presents the incoming ion count rate, which can be regarded as the total number of registered emission events in a non-coincidence spectrum (e.g. area below the blue curve in Figure 4.1), divided by the measurement time.

Observing now spectra received from bombardment of the Quantifoil sample with argon ions at different charge states and impact energies leads to the conclusion that the resulting EES from a performed coincident measurement cannot only originate from random coincidences. Table 4.1 includes the percentages of emission events caused by random and true coincidences calculated by means of Equation 4.1 for Ar^{q+} bombardment of the Quantifoil target. The extremely high fraction of true coincidences reveals that even for ions at low-charge states, and with low impact energies a thickness of 20 nm (10 nm carbon layer and 10 nm polyvinyl formal) is only marginally effective in preventing the projectiles from traversing the support. Comparing the random to true coincidences ratio for SLG (cf. Table 4.2) exhibits a clearly higher percentage of true coincidences for SLG as for the Quantifoil target. Unfortunately for the interpretation of emission yields from graphene received by coincidence measurements in the following Sections, we have to consider that these electrons are not coming from freestanding SLG alone, but include significant contributions from SLG plus Quantifoil support.

Table 4.1: Determined percentages of emission events caused by random and true coincidences for bombarding a Quantifoil target with Ar^{q+} ions derived from experimental count rates. For calculating the probability for random coincidences a gate width of $T=2 \mu\text{s}$ was assumed. The random coincidences are calculated by multiplying the measured count rate registered at the MCP I_g with the calculated probability W_i for an ion to reach the sample while the gate of the previous one is still opened ($I_c^{\text{rand}} = I_g \cdot W_i$). To obtain the rate of random coincidences in the measured spectra, this value is compared to the actually measured coincidence count rate I_c^{meas} in the following way: $(I_g \cdot W_i)/I_c^{\text{meas}}$. The percentage of true coincidences is therefore: true coinc = 1 - random coinc.

Ar^{q+}	E_{kin}	I_i	I_c^{meas}	I_g	W_i	I_c^{rand}	random coinc	true coinc
Ar^{2+}	12 keV	6969	57	320	0.02	4.4	7.8%	92.2%
Ar^{3+}	12 keV	12074	112	700	0.02	16.7	14.9%	85.1%
Ar^{4+}	12 keV	15710	79	500	0.03	15.5	19.5%	80.6%
Ar^{5+}	12 keV	17104	136	750	0.03	25.2	18.5%	81.5%
Ar^{6+}	12 keV	7942	248	800	0.02	12.6	5.1%	94.9%
Ar^{7+}	12 keV	9710	80	550	0.02	10.6	13.3%	86.7%
Ar^{8+}	12 keV	7881	56	250	0.02	3.9	7.0%	93.1%
Ar^{9+}	12 keV	8557	171	600	0.02	10.2	5.9%	94.1%
Ar^{2+}	2 keV	15492	352	774	0.03	23.6	6.7%	93.3%
Ar^{9+}	54 keV	5410	57	309	0.03	9.9	17.3%	82.7%

4.2 Comparison of electron yields for ion bombardment of SLG and C-foils

Investigating electron emission induced by slow multiply and highly charged ions helps to improve the understanding of fundamental ion-surface interactions. Especially the neutralization process upon surface impact is of great interest, and strongly depends on properties like the energy band gap and the work function of the target material. In general, the obtained electron emission yield results from both the KE as well as the PE, even though there exists a threshold velocity v_{th} for the onset of kinetic electron emission due to direct momentum transfer within the collision system (see Section 1.2 for a more detailed description). KE originates from the transfer of projectile energy to the electronic system of the target and therefore arises from within the solid bulk [11]. For subsequent electron emission the escape through the surface-vacuum boundary requires therefore a minimum velocity. The electron yield due to γ_{KE} is proportional to the geometric path-length of the ion within the electron escape zone and scales consequently with $\cos(\vartheta)^{-1}$ [11] as it is presented in Equation 1.9,

Table 4.2: Contributions in the emission spectrum of random and true coincidences for bombarding SLG mounted on its Quantifoil support with Ar^{q+} ions. For calculating the probability for random coincidences again a gate width $T=2 \mu\text{s}$ was assumed and the calculation procedure was the same as presented in Table 4.1.

Ar^{q+}	E_{kin}	I_i	I_c^{meas}	I_g	W_i	I_c^{rand}	random coinc	true coinc
Ar^{2+}	12 keV	8687	110	270	0.02	4.7	4.2%	95.8%
Ar^{3+}	12 keV	11481	294	600	0.02	13.6	4.6%	95.4%
Ar^{4+}	12 keV	15942	241	500	0.03	2.4	6.5%	93.5%
Ar^{5+}	12 keV	20028	348	500	0.04	3.5	6.3%	93.8%
Ar^{6+}	12 keV	9515	353	700	0.02	13.2	3.7%	96.3%
Ar^{7+}	12 keV	10776	251	400	0.02	8.5	3.4%	96.6%
Ar^{8+}	12 keV	7676	90	190	0.02	2.9	3.2%	96.8%
Ar^{9+}	12 keV	4271	42	120	0.01	1.0	2.4%	98.0%
Ar^{2+}	2 keV	13635	309	730	0.03	19.6	6.4%	93.6%
Ar^{9+}	54 keV	18565	659	722	0.03	26.3	4.0%	96.0%

with ϑ representing the impact angle. Above the threshold v_{th} an approximately linear increase in the kinetic emission yield is expected in accordance with the electronic stopping power (cf. Equation 1.8). Deviations from this proportionality are typically of the order of 10 % for protons incident on thick metallic targets in a large energy range [11]. Baragiola *et al.* [69] have already proposed an approximate value for the material dependent constant $\Lambda^{\text{ex}} \approx 0.1 \text{ \AA eV}$, which seems to be correct within 30 % for a hugh variety of metal and semiconductor targets [70]. Due to its potential energy the neutralization process for the projectile will already start above the surface, giving rise to PE contributions to the total electron emission yield. The number of emitted electrons depends on the interaction time above the surface, and therefore scales therefore inversely with the ion velocity. Considering a velocity-independent contribution of the total emission yield γ_{∞} attributed to the "peeling-off effect" [19] at the surface selvedge, γ_{PE} can be approximated by the empirical relation presented in Equation 1.5 according to [13, 19, 35, 39–41].

By summing up both contributions from kinetic, as well as potential emission the total electron emission yield γ for the impact of a multiply charged ion on a solid can be approximated as [11, 13, 24, 39]:

$$\gamma(v, \vartheta) = \gamma_{PE} + \gamma_{KE} = \underbrace{\frac{c_{PE}}{\sqrt{v \cdot \cos(\vartheta)}}}_{\gamma_{PE}} + \gamma_{\infty} + \underbrace{\Theta(v - v_{th}) \frac{c_{KE}(v - v_{th})}{\cos \vartheta}}_{\gamma_{KE}}, \quad (4.3)$$

for an ion-beam impact angle ϑ with respect to the surface normal. In Equation 4.3 c_{PE} and c_{KE} are proportionality factors for PE and KE contributions, respectively while $\Theta(v - v_{th})$ is a Heaviside step function governing the onset of the kinetic electron emission above the threshold velocity v_{th} . It was interesting to see, whether this empirical relation 4.3 holds for SLG targets as well.

To completely separate these two regimes either slow ions at very high charge states or projectiles with velocities below the threshold v_{th} would be necessary for reaching the PE-dominated regime, while neutral projectiles would lead to emission yields resulting from pure KE. Since the velocity of the ions depends on the adjusted extraction voltage (Equation 2.3). The separation between these two regimes is hard to reach due to limitations in the available voltage range of the ECR ion source ($1 \text{ kV} \lesssim U \lesssim 6 \text{ kV}$). Additionally, the usage of SOPHIE is accompanied by constraints in the reachable argon ion charge state ($1 \leq q \leq 14$).

For obtaining the desired electron emission results the targets of interest were bombarded with Ar ions ($2 \leq q \leq 9$) in an energy range of 2–54 keV, which leads to the following velocity limitations:

$$v_{\min}(2 \text{ keV}) = 9.8 \times 10^4 \text{ m/s},$$

and

$$v_{\max}(54 \text{ keV}) = 51 \times 10^4 \text{ m/s}.$$

4.2.1 Dependence on the projectile velocity

In order to gather the first velocity dependent electron emission yield from single layer graphene the target was bombarded with Ar^{2+} and Ar^{9+} ions. Due to the energy limitations given by the ECRIS the projectile velocity was confined to $9.8 \times 10^4 \leq v \leq 24.1 \times 10^4 \text{ m/s}$ in the case of Ar^{2+} and to $20.8 \times 10^4 \leq v \leq 51 \times 10^4 \text{ m/s}$ for Ar^{9+} . All presented results were obtained for ion bombardment under an impact angle of $\vartheta = 45^\circ$ with respect to the surface plane. Hence, no evaluation of the electron yield dependence on the incident angle was feasible which is strongly suggested here for future electron yield studies since it expands the possibility for PE and KE separation. Equation 4.3 can be simplified as

$$\gamma(v) = \underbrace{\gamma_{PE}}_{\frac{\tilde{c}_{PE}}{\sqrt{v}} + \gamma_\infty} + \underbrace{\Theta(v - v_{th}) \tilde{c}_{KE} (v - v_{th})}_{\gamma_{KE}}, \quad (4.4)$$

where

$$\tilde{c}_{PE} = \frac{c_{PE}}{\sqrt{\cos \vartheta}} = \frac{c_{PE}}{\sqrt{\cos(45)}}, \quad (4.5)$$

and

$$\tilde{c}_{KE} = \frac{c_{KE}}{\cos \vartheta} = \frac{c_{KE}}{\cos(45)}. \quad (4.6)$$

A deterioration in the collection efficiency for the applied measurement setup for decreasing impact angle was found [29] but for the selected angle of $\vartheta = 45^\circ$ no correction in the yield was necessary. The determined electron emission yields from SLG bombarded with Ar^{2+} and Ar^{9+} ions with varying velocities under an impact angle of $\vartheta = 45^\circ$ with respect to the surface plane are presented in Figure 4.4 (green data points).

The measured electron emission yields as a function of projectile velocity can be nicely fitted – according to Equation 1.8 – by a linear function. This leads to the obvious conclusion that the projectile velocities lie already above the kinetic threshold. The value of this threshold strongly depends on quantities of the target material such the Fermi energy and the work function [23] (cf. Equation 1.7).

It is interesting to compare the results for single layer graphene with results for materials of similar characteristics was considered. Therefore results for ion-induced electron emission from HOPG [71, 72] are represented as well in Figure 4.4. Such highly pure and ordered form of graphite consists of well-defined layered carbon sheets which leads to high electrical conductivity parallel to these layers compared to the perpendicular direction [73]. Since the two-dimensional graphene is regarded as a very good conductor, results obtained by argon ion impact on HOPG parallel to these carbon sheets were taken into consideration. Cernusca received in his PhD thesis [71] the total electron emission yield for Ar^+ bombardment of HOPG under normal incident at different ion velocities. For comparing these results with the measurements performed under an impact angle of $\vartheta = 45^\circ$ the yield γ determined by [71] was corrected for the difference in impact angle by means of Equation 1.9.

Bodewits *et al.* [72] measured the electron yields for highly charged ions (Ar and Xe) impinging on HOPG as a function of projectile velocity just above the kinetic threshold. The results for Ar^{13+} under an impact angle of $\vartheta=45^\circ$ with respect to the surface normal (data for $\vartheta=30^\circ$ were again corrected by means of Equation 1.9) are also represented in Figure 4.4. The emission yield for Ar^{9+} was only obtained for one specific impact velocity but as a matter of guidance this data point is included as well to the sake of completeness.

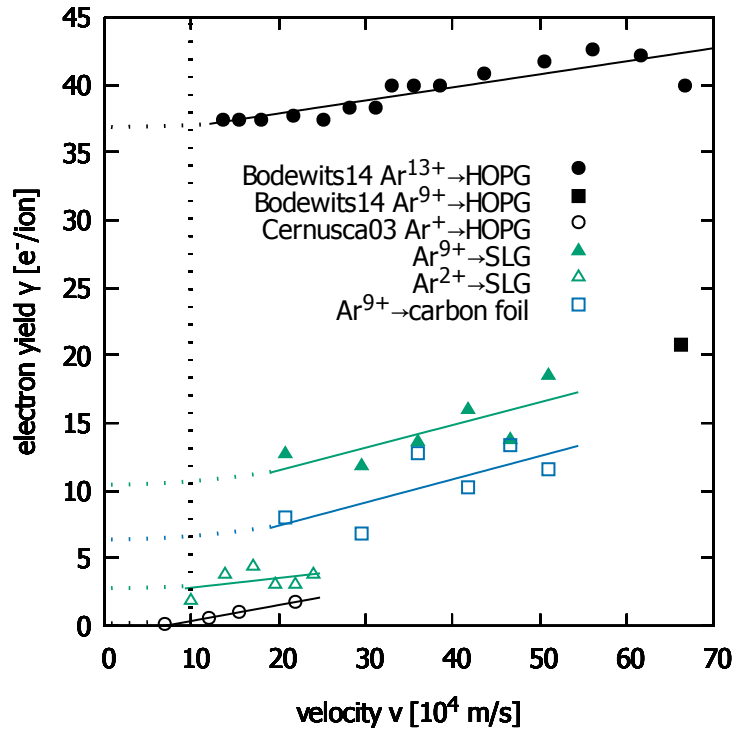


Figure 4.4: Velocity dependence of emission yield from SLG and carbon foils bombarded with Ar^{q+} ions under an impact angle of $\vartheta = 45^\circ$. Total electron yields from HOPG measured by [72] and [71] have been added for comparison. The dashed vertical line indicates the threshold velocity for HOPG found by [74]. All data points were fitted by a linear fit function depending on an offset caused by PE and a proportionality factor for the KE contribution. In the PE-dominant regime below the threshold for kinetic electron emission the velocity dependence is just continued as a matter of guidance. Due to PE the electron yield for projectiles at charge states $q \geq 3$ is expected to rise again with decreasing impact velocity but no data were available by these measurements.

According to Equation 1.7, Cernusca *et al.* [74] calculated the threshold velocity for HOPG by considering a target work function of 5.0 eV and 21.3 eV for the Fermi energy [75]. They determined a KE threshold of $v_{\text{th}}(\text{C}) \approx 15 \times 10^4$ m/s while their performed measurements led to a slightly lower value for HOPG ($v_{\text{th}}(\text{C}) \approx 10 \times 10^4$ m/s). Such deviation from the calculated v_{th} might be related to the band structure of the material which is assumed to be the one of a quasi-free electron metal in Equation 1.7, and an additional surface assisted KE mechanism caused by partial localisation of the quasi-free electrons [74, 76, 77].

The exact KE threshold value for single layer graphene is unknown but, since HOPG can be regarded as a composition of many graphene layers, the assumption of similar threshold velocities seems to be appropriate. The dashed vertical line in Figure 4.4 indicates the threshold value found for HOPG in [74] and assumed for SLG. Since the received electron emission yields for both Ar^{2+} and Ar^{9+} increase linearly with the projectile velocity a nearly constant potential emission contribution in this energy range is presumed. Equation 4.4 can then be reduced to an expression with a reduced number of parameters as

$$\gamma(v) = \gamma_{PE}^{\infty} + \tilde{c}_{KE} \cdot (v - v_{th}), \quad (4.7)$$

where γ_{PE}^{∞} results from an offset caused by PE below the threshold, and \tilde{c}_{KE} represents the KE proportionality factor.

In addition to the comparison of SLG with HOPG the same measurement procedure was performed for amorphous thin carbon foils with an areal density of $5 \mu\text{m}/\text{cm}^2$ (purchased from Arizona Foil Company). Under an impact angle of $\vartheta = 45^\circ$ with respect to the surface normal the carbon foils were bombarded with Ar^{2+} within a velocity range of $9.8 \times 10^4 \leq v \leq 24.1 \times 10^4 \text{ m/s}$ and Ar^{9+} within a velocity range of $20.8 \times 10^4 \leq v \leq 51 \times 10^4 \text{ m/s}$. Figure 4.4 includes the results obtained for Ar^{9+} induced electron emission from such carbon foil targets (blue data points) to compare them with the findings for SLG and HOPG. Due to very low emission yields received from the measurements with Ar^{2+} the evaluation of these spectra was governed by huge errors and therefore the results were not added at this point.

Cernusca *et al.* [77] measured kinetic emission from carbon tiles as well as from HOPG induced by different projectiles and concluded a similarity in the KE threshold velocities for both targets. Hence the threshold velocity $v_{th}(C) \approx 10 \times 10^4 \text{ m/s}$ for HOPG represented by the dashed line in Figure 4.4 was assumed to count as an indication for the threshold velocity for our carbon foils as well. Accordingly all presented data points lie above the assumed KE threshold and as a consequence the received emission yields are once more fitted by the kinetic emission contribution (cf. Equation 4.7).

Table 4.3 presents the determined fit parameters γ_{PE}^{∞} and \tilde{c}_{KE} for both target materials, as well as those for HOPG obtained by fitting the data of [71] and [72] by means of Equation 4.7. For all targets a threshold velocity of $10 \times 10^4 \text{ m/s}$ was assumed.

By analyzing the obtained fit parameters one can conclude a clear increase of the yield with projectile velocity and a potential electron emission yield γ_{PE}^{∞} increasing

Table 4.3: Derived fit parameters for Ar^{q+} bombardment of different targets. γ_{PE}^∞ represents the velocity independent PE contribution while \tilde{c}_{KE} comprises the proportionality factor for KE.

target	projectile	γ_{PE}^∞	\tilde{c}_{KE}
HOPG	Ar^{13+}	36.4	0.13
SLG	Ar^{9+}	9.8	0.17
C-foil	Ar^{9+}	5.7	0.17
SLG	Ar^{2+}	2.8	0.07
HOPG	Ar^+	0.4	0.17

with charge states. The dependence on the kinetic energy of the projectile seems to be almost the same for all target materials although the smaller slope represented by \tilde{c}_{KE} in the case of Ar^{2+} bombardment of SLG indicates a weaker dependency. This might be caused by the above mentioned much higher errors in the evaluation for low yield spectra.

The comparison of the electron yield for Ar^{9+} impinging on graphene and amorphous carbon indicates a much higher emission yield for SLG than for the considerably thicker carbon foil. The results presented in Table 4.3 lead to a difference in the potential emission yields of $\Delta\gamma_{PE}^\infty \approx 4.1 e^-$ for these two targets. However, one has to consider that the higher yield in the case of SLG might also arise from electrons emitted from the back side of the SLG target. Due to the one atom thickness of this special two-dimensional material such electrons might have the possibility to be accelerated through the sample onto the PIPS detector and therefore add to the received emission yield. A way to overcome this problem might be a slightly positively biased electrode close to the back side of the target for extracting the electrons ejected from the back side. At this point it has to be clearly emphasized that the received coincidence EES from SLG not only originates from graphene but also from its supporting Quantifoil since neither the Ar^{2+} not the Ar^{9+} projectile can be sufficiently stopped.

The performed coincidence measurements were only the very first attempt for collecting information on ion-induced electron emission from graphene. Results of emission yields from SLG were obtained for a variety of projectile velocities under a fixed impact angle. For extending the investigations on PE and KE resulting from ion bombardment of graphene further measurements have been performed as elaborated in more detail in the following chapter.

4.2.2 Charge state dependency

As it was already presented above (cf. Section 4.2.1) a strong increase in the electron emission yield with the projectile charge state q exists if one compares the results for Ar^{2+} and Ar^{9+} impinging on the same target. Related to the charge state is the potential energy $W_{pot}(q)$ an ion is carrying towards the surface. $W_{pot}(q)$ is determined by the sum of ionization energies E_i , which have to be spent to remove q electrons from the initially neutral atom during the ion production process

$$W_{pot}(q) = \sum_{n=1}^q E_i^n. \quad (4.8)$$

The increase of the potential energy $W_{pot}(q)$ is not linear with the charge state q , but rather reflects the shell structure of the ion. Its dependence as a function of charge state q is demonstrated in Figure 4.5 for the case of argon ions which is the ion species in our measurements.

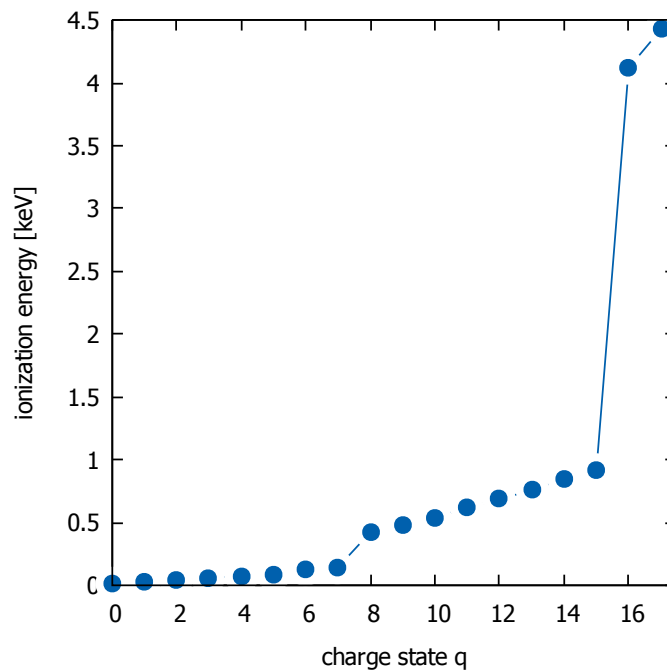


Figure 4.5: Ionization energy as a function of charge state for argon. The clearly visible steps in this trend indicate the higher ionization energy that is required for removing electrons from the L and K shell.

Ar ions of charge state $q \leq 8$ have completely filled K and L shells, whereas for projectiles with $q > 8$ the number of L shell vacancies increases. While at lower charge

states only weakly-bound electrons from the M shell have to be removed, the higher charge states require a higher ionization energy for the creation of L-shell vacancies. As a result a much higher incremental increase of the secondary-electron yields for argon projectiles with $q > 8$ [72] has to be expected, and can be observed in the electron emission results of SLG performed within this work.

Charge state depending emission yields for impact of 12 keV Ar^{q+} ($q = 2, 3, \dots, 9$) on SLG and thin carbon foils at an incident angle of $\vartheta=45^\circ$ with respect to the surface normal were obtained. Figure 4.6 presents the increase in the total electron emission yield with the ion charge state for the performed measurements. Since the 20 nm thick Quantifoil support film consists at least of a 10 nm carbon layer according to specifications of the manufacturer [56] for the purpose of comparison the obtained emission yields for this carbon-based material were added in Figure 4.6. For all performed measurements in the present work (blue data points in Figure 4.6) the kinetic energy of the Ar^{q+} projectiles was kept at 12 keV and the impact angle was set to 45° with respect to the incoming ion beam. Bodewits *et al.* [72] showed the charge state dependency for Ar^{q+} bombardment of HOPG at different incidence angles. Their results for $\vartheta = 45^\circ$ are included in Figure 4.6, even though they used projectiles at a much higher impact energy (91 keV). The broad gap in the emission yield received from Ar^{9+} compared to Ar^{8+} can be clearly observed for all targets and is attributed to the removal of the stronger bound electrons from the L shell in the case of Ar^{9+} .

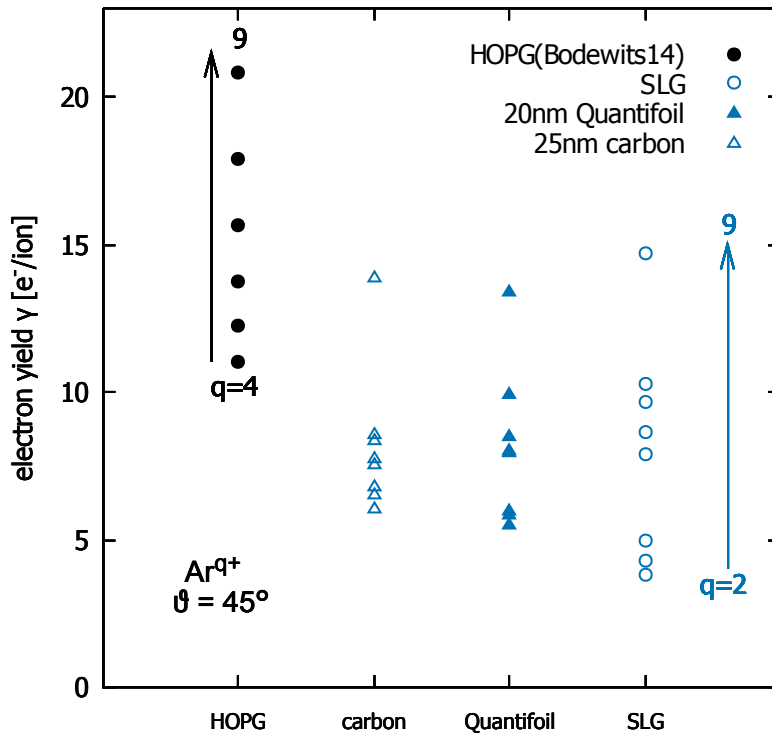


Figure 4.6: Shell structure of the projectile ion represented in the total electron emission yield. The high increase in the yield for argon ions at the charge state $q=9$ is reasoned on the higher required ionization energy that has to be spent into the creation of L shell vacancies. The figure includes measured emission results for SLG, its Quantifoil support and amorphous carbon for the bombardment with 12 keV argon ions. Electron yields for HOPG received by [72] with 91 keV Ar ions have been included for comparison.

With the assumption that the kinetic electron emission at the considered energy (12 keV) is independent from the ion charge state the difference in the total electron yield for ions at different charge states and fixed kinetic energy can be solely assigned to potential electron emission. Calculating now the difference between the total electron yield gained for the highest charge state $q = 9$ and the lowest charge state $q = 2$ leads to an insight in PE for the different targets. Table 4.4 presents the results for this determination. In accordance to the results of the previous Section SLG again shows a much higher electron yield than amorphous carbon.

Usually a linear increase of the PE yield with the potential energy W_{pot} is assumed for low charge states, as it has been noted by different authors [19, 78, 79]. In Figure 4.7 the measured electron yield has been plotted versus the available potential

Table 4.4: PE contribution to the total electron yield in comparison for different targets bombarded with 12 keV Ar ions.

target	$\Delta\gamma_{PE}(q_{max} - q_{min})$
C-foil	7.3
Quantifoil	7.9
SLG	10.9

energy W_{pot} carried by 12 keV Ar ions. For $q \leq 8$ charge states the authors in [19] claim that the slope of the curve fitted to the γ values corresponds to the energy required for the emission of one electron. For charge states $q \geq 9$ the yields may again be fitted by a straight line but the slope changes due to higher "cost" for emitting each additional electron at this projectile charge state. Argon ions with charge states $q \leq 8$ have completely filled K and L shells, whereas an increasing number of L-shell vacancies show up for charge states above. If there is not sufficient time to fill up these vacancies before the projectile reaches the surface, there will still be q electrons in the M shell or higher shells as well as $(q - 8)$ vacancies in the L-shell. As a result the energy stored in these $(q - 8)$ highly excited projectiles has not yet been available for slow electron emission in the RN-AI deexcitation cascades above the surface. In the present work Ar charge states $q > 9$ were not available and all yield data can still be fitted with a linear dependence on W_{pot} (see Figure 4.7).

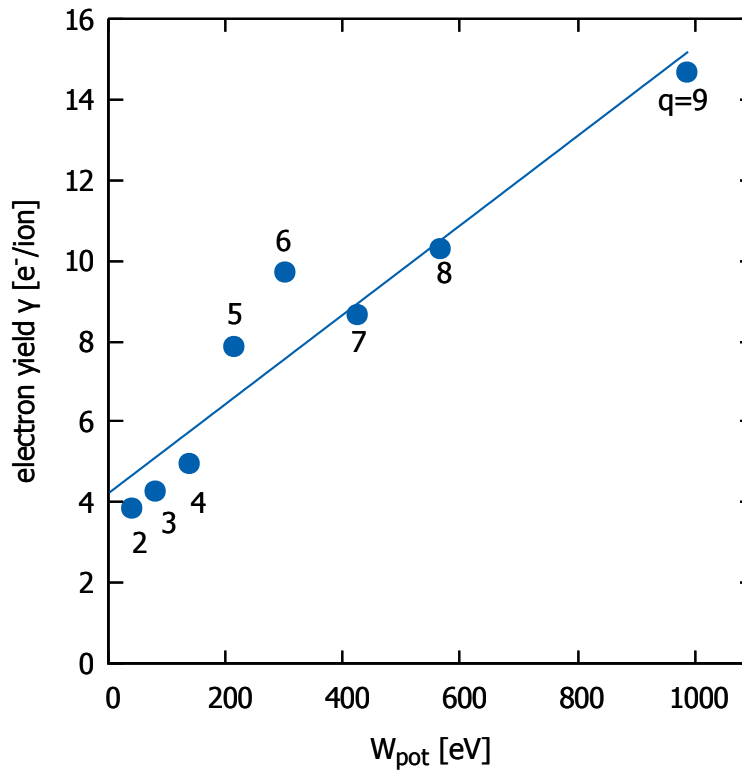


Figure 4.7: Electron yield dependence on the potential energy W_{pot} carried by 12 keV Ar^{q+} ions impinging – under an impact of 45° with respect to the surface normal – on SLG. The potential energy necessary for emission of one electron due to potential emission is on the average about 88 eV, a value very well comparable to metallic surfaces like Au or W [19, 78].

5 Conclusion & Outlook

Electron emission from metal [17–20] and insulator [21, 22] surfaces has been already investigated at the TU Wien for decades. With the access to the ultimately thin two-dimensional material graphene, especially single layer graphene provided by our coworkers at the University of Duisburg-Essen, investigations of its interaction with multiply charged ions became of great interest for a better understanding of the underlying physical processes.

For separating emission events originating from ion transmission through SLG from ion impact on its support, coincidence measurements were attempted in this master thesis and a corresponding experimental setup was built. Comparing the results for coincident and non-coincidence ion-induced electron emission from graphene indeed showed differences in the received total electron yields.

Based on the EES evaluation method proposed in [17, 18] a computer script was developed for ensuring an automatic yield calculation from electron emission spectra [68].

Investigations on kinetic and potential electron emission from SLG were accomplished by individually varying the charge state of the impinging ion and keeping the velocity fixed as well as diversifying the impact velocity at a constant charge state. The dependence of the yield on the incident velocity was compared to previous measurements of ion-induced electron emission from HOPG [71, 72] partly performed at the TU Wien. The measured yields for both the HOPG as well as the SLG were described in good agreement by the well known empirical relations including contributions of KE and PE.

As a further step, the velocity independent fraction of the potential electron emission was compared for SLG and thin carbon foil. As a surprising result a much higher PE yield was found for this two-dimensional allotrope of carbon.

Measuring EES for the examined target materials exposed a clear yield dependence on the charge state (or the potential energy) of the ion as it was expected for the dominant potential emission process.

Receiving non-negligible high yield coincident spectra for the Quantifoil target alone lead to the conclusion that the projectile ions in this energy range are able to traverse the carbon-based support. The obtained pulse height distribution could not be justified by only originating from random coincidences according to the performed estimations. Consequently, a thickness of 20 nm Quantifoil (10 nm carbon layer and 10 nm polyvinyl formal) is found to be not sufficiently thick to stop 2-54 keV Ar^{q+} ions. Coincidence measurements of ion-induced electron emission are therefore not able to separate electrons originating from freestanding SLG and those from SLG on the Quantifoil support. For improving future coincident recordings first and foremost a different carrier for graphene should be considered. Quantifoils additionally evaporated with 100 nm gold can serve as an adequate supporting material since the resulting thickness of 120 nm should be sufficiently thick to stop argon ion projectiles with energies up to 100 keV according to SDTRIM.SP simulations. The calculated stopped fraction per penetration depth for 60 keV and 100 keV projectiles is shown in Figure 5.1).

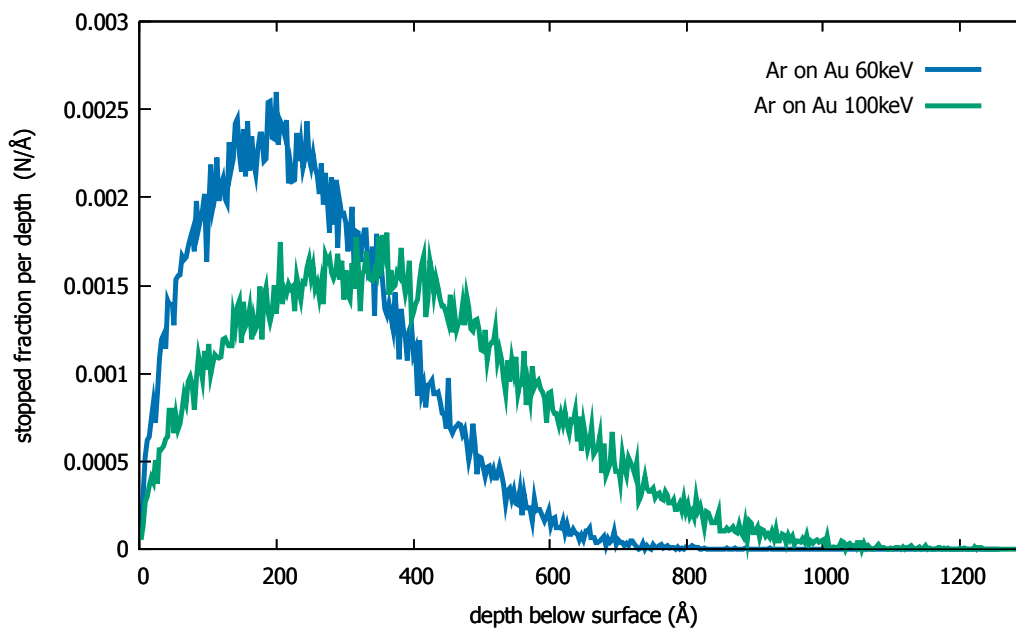


Figure 5.1: SDTRIM.SP simulation (performed by Bernhard Berger) presenting the stopped fraction per depth for argon impinging on gold. 100 nm Au layer on top of the Quantifoil is therefore expected to be sufficient for stopping both 60 keV as well as 100 keV argon projectiles.

Once the graphene is mounted on an appropriate support a range of further investigations on its ion-induced emission yield can be considered. Recording EES at different impact angles with projectile velocities below the kinetic threshold would help

to determine the missing fit parameters c_{PE} and γ_{PE}^{∞} in the PE regime, and finally the total electron yield could be fitted by the expression presented in Equation 4.3 within the whole velocity range. Observing the resulting emission spectra for bombardment with different ion species would improve the understanding of ion-graphene interaction processes. In addition the implementation of a different ion source would enlarge the range of impact energies and charge states and thus even velocities in the pure PE regime would be accessible. This will become feasible when applying an electron beam ion source (EBIS), which is currently planned for future measurements on EES from SLG. The EBIS will enable the production of fully stripped Xe^{54+} and Ar^{18+} ions.

Concerning the possibility for electrons emitted from the back side of the single layer graphene getting extracted by the high voltage applied to the PIPS detector and therefore increasing the gathered EES, for future measurement procedures a modified extraction electrode for this disturbing electrons is suggested. Another advisement is to examine EES from the back side of the sample by rotating the sample holder in a way that its back side is facing the collection grid. Comparing the results to the ones received from the front side might give a deeper insight in the electron producing processes within the graphene layer. In addition to the already ongoing transmission measurements of slow MCI and HCI through free-standing few atomic layer films [80, 81] the coincidence measurements of ion-induced electron emission from graphene are planned to be supplemented with energy loss and charge loss evaluations. Combining the study on electron emission, charge exchange and energy loss for two-dimensional materials like graphene will imply a further step in ion-matter investigations.

List of Figures

Figure 1.1	Total electron emission yield vs. impact velocity	3
Figure 1.2	Different processes involved in hollow atom-formation and -decay	5
Figure 1.3	Resonant electronic transitions	6
Figure 1.4	Auger neutralisation	7
Figure 1.5	Auger de-excitation	8
Figure 1.6	Auto ionisation	9
Figure 2.1	Main components of an ECRIS for production of MCI	15
Figure 2.2	The ion beam facility at the Vienna University of Technology	17
Figure 2.3	Drawing of the electrostatic einzel lens with the attached pair of deflection plates	18
Figure 2.4	Schematic of the most important elements the ions pass on their way through the beamline	19
Figure 2.5	Schematic of the collision chamber	20
Figure 2.6	Sample holder for multiple target investigation	21
Figure 2.7	Principle of a microchannel plate detector	22
Figure 2.8	Drawing of a PIPS detector	23
Figure 2.9	Honeycomb structure of graphene	25
Figure 2.10	Graphene supporting Quantifoil-TEM grid	25
Figure 2.11	Graphene and support sample positioned in the slots of the target holder	26
Figure 2.12	Preparation process for carbon foil targets.	27
Figure 2.13	Carbon foil samples positioned in the slots of the target holder	28
Figure 2.14	SDTRIM.SP simulation for Ar penetrating C	29
Figure 2.15	Schematic of the electronics used in the performed coinci- dence measurements	31
Figure 2.16	Calibration of MCA channels	35
Figure 3.1	Contributions of m out of n backscattered electrons to the normalized Gauss function $F_4(E)$	40
Figure 3.2	The intrinsic detector noise peak covering the peak repre- senting the emission of one electron	42

Figure 3.3	Calibration by the Python routine	43
Figure 3.4	Background subtraction procedure	44
Figure 3.5	Direct determination of fitting parameters C_n	46
Figure 3.6	Determination of fitting parameters C_n by assuming two Poisson distribution	47
Figure 3.7	Determination of fitting parameters C_n by assuming three Poisson distribution	48
Figure 3.8	Results of the performed evaluation procedure	49
Figure 4.1	Comparison of coincident and non-coincidence spectra	52
Figure 4.2	Probabilities W_n for the emission of n electrons induced by ion impact	53
Figure 4.3	Charge state dependence of the electron emission yield for coincidence and non-coincidence EES	54
Figure 4.4	Velocity dependence of the emission yield from the examined target materials	60
Figure 4.5	Ionization energy as a function of charge state for Argon	63
Figure 4.6	Shell structure of the projectile ion represented in the emission yield	65
Figure 4.7	Yield dependence on potential energy W_{pot}	67
Figure 5.1	SDTRIM.SP simulation for Ar penetrating a Au surface	70

Bibliography

- [1] M. Gasparotto, R. Andreani, L. V. Boccaccini, A. Cardella, G. Federici, L. Giancarli, G. L. Marois, D. Maisonnier, S. Malang, A. Moeslang, Y. Poitevin, B. van der Schaaf, and M. Victoria. *Survey of in-Vessel Candidate Materials for Fusion Power Plants - the European Materials R&D Programme*. *Fusion Engineering and Design* **66 - 68**, 129 (2003).
- [2] M. Shimada, A. E. Costley, G. Federici, K. Ioki, A. S. Kukushkin, V. Mukhovatov, A. Polevoi, and M. Sugihara. *Overview of Goals and Performance of ITER and Strategy for Plasma-Wall Interaction Investigation*. *Journal of Nuclear Materials* **337 - 339**, 808 (2005).
- [3] G. Federici. *Plasma Wall Interactions in ITER*. *Physica Scripta* **T124**, 1 (2006).
- [4] A. K. Geim and K. S. Novoselov. *The rise of graphene*. *Nat Mater* **6**, 183 (2007).
- [5] J. S. Bunch, S. S. Verbridge, J. S. Alden, A. M. van der Zande, J. M. Parpia, H. G. Craighead, and P. L. McEuen. *Impermeable Atomic Membranes from Graphene Sheets*. *Nano Lett.* **8**, 2458 (2008).
- [6] V. Berry. *Impermeability of graphene and its applications*. *Carbon* **62**, 1 (2013).
- [7] L. Tsetseris and S. Pantelides. *Graphene: An impermeable or selectively permeable membrane for atomic species?* *Carbon* **67**, 58 (2014).
- [8] Y. Cui, S. Kundalwal, and S. Kumar. *Gas barrier performance of graphene/polymer nanocomposites*. *Carbon* **98**, 313 (2016).
- [9] M. Rösler, W. Brauer, J. Devooght, J.-C. Dehaes, A. Dubus, M. Cailler, and J.-P. Ganachaud. *Particle Induced Electron Emission I*. *Springer Tracts in Modern Physics* **122** (1991).
- [10] G. Spierings, I. Urazgil'din, P. A. Zeijlmans van Emmichoven, and A. Niehaus. *Identification of the Mechanism for Kinetic Emission in keV Proton Cu(110) Collisions*. *Phys. Rev. Lett.* **74**, 4543 (1995).
- [11] D. Hasselkamp, H. Rothard, K. O. Groeneveld, J. Kemmler, P. Varga, and H. Winter. *Particle Induced Electron Emission II*, vol. 123 of *Springer Tracts in Modern Physics*. Springer Berlin, Heidelberg (1992).

- [12] H. Winter. *Slow Heavy-Particle Induced Electron Emission from Solid Surfaces*, vol. 225 of *Springer Tracts in Modern Physics*, chap. Kinetic Electron Emission for Grazing Scattering of Atoms and Ions from Surfaces. Springer Berlin, Heidelberg (2007).
- [13] F. Aumayr and H. P. Winter. *Slow Heavy-Particle Induced Electron Emission from Solid Surfaces*, vol. 225 of *Springer Tracts in Modern Physics*, chap. Potential Electron Emission from Metal and Insulator Surfaces. Springer Berlin, Heidelberg (2007).
- [14] H. D. Hagstrum. *Electron Ejection from Ta by He^+ , He^{++} , and He_2^+* . Phys. Rev. **91**, 543 (1953).
- [15] H. D. Hagstrum. *Auger Ejection of Electrons from Tungsten by Noble Gas Ions*. Physical Review **96**, 325 (1954).
- [16] H. D. Hagstrum. *Auger Ejection of Electrons from Molybdenum by Noble Gas Ions*. Phys. Rev. **104**, 672 (1956).
- [17] G. Lakits, F. Aumayr, and H. Winter. *Statistics of ioninduced electron emission from a clean metal surface*. Review of Scientific Instruments **60**, 3151 (1989).
- [18] F. Aumayr, G. Lakits, and H. Winter. *On the measurement of statistics for particle-induced electron emission from a clean metal surface*. Applied surface science **47**, 139 (1991).
- [19] H. Kurz, F. Aumayr, C. Lemell, K. Töglhofer, and H. Winter. *Neutralization of slow multicharged ions at a clean gold surface: Total electron yields*. Physical Review A **48**, 2182 (1993).
- [20] C. Lemell, J. Stöckl, J. Burgdörfer, G. Betz, H. Winter, and F. Aumayr. *Multicharged ion impact on clean Au (111): Suppression of kinetic electron emission in glancing angle scattering*. Physical review letters **81**, 1965 (1998).
- [21] M. Vana, F. Aumayr, P. Varga, and H. Winter. *Electron emission from polycrystalline lithium fluoride bombarded by slow multicharged ions*. Nuclear Instruments and Methods in Physics Research Section B: Beam Interactions with Materials and Atoms **100**, 284 (1995).
- [22] M. Vana, F. Aumayr, P. Varga, and H. P. Winter. *Electron Emission from Polycrystalline Lithium Fluoride Induced by Slow Multicharged Ions*. EPL (Europhysics Letters) **29**, 55 (1995).
- [23] R. A. Baragiola, E. V. Alonso, and A. O. Florio. *Electron emission from clean metal surfaces induced by low-energy light ions*. Phys. Rev. B **19**, 121 (1979).

- [24] H. Eder, F. Aumayr, and H. Winter. *Search for projectile charge dependence of kinetic electron emission from clean polycrystalline gold*. Nuclear Instruments and Methods in Physics Research Section B: Beam Interactions with Materials and Atoms **154**, 185 (1999).
- [25] J. Stöckl, T. Suta, F. Ditroi, H. Winter, and F. Aumayr. *Separation of Potential and Kinetic Electron Emission for Grazing Impact of Multiply Charged Ar Ions on a LiF(001) Surface*. Phys. Rev. Lett. **93**, 263201 (2004).
- [26] E. Bodewits, H. Bekker, A. de Nijs, R. Hoekstra, D. Winklehner, B. Daniel, G. Kowarik, K. Dobes, and F. Aumayr. *Electron emission yields from boron-like Ar ions impinging on Au(1 0 0)*. Nuclear Instruments and Methods in Physics Research Section B: Beam Interactions with Materials and Atoms **269**, 1203 (2011).
- [27] A. Arnau, F. Aumayr, P. Echenique, M. Grether, W. Heiland, J. Limburg, R. Morgenstern, P. Roncin, S. Schippers, R. Schuch, N. Stolterfoht, P. Varga, T. Zouros, and H. Winter. *Interaction of slow multicharged ions with solid surfaces*. Surface Science Reports **27**, 113 (1997).
- [28] J. Burgdörfer, P. Lerner, and F. W. Meyer. *Above-surface neutralization of highly charged ions: The classical over-the-barrier model*. Phys. Rev. A **44**, 5674 (1991).
- [29] M. C. Simon. *Elektronen-Emission bei Beschuss von Isolator- und Metall-Oberflächen mit hochgeladenen Ionen*. Master's thesis, Vienna University of Technology (2006).
- [30] H. D. Hagstrum. *Theory of Auger Ejection of Electrons from Metals by Ions*. Physical Review **96**, 336 (1954).
- [31] H. Ryufuku, K. Sasaki, and T. Watanabe. *Oscillatory behavior of charge transfer cross sections as a function of the charge of projectiles in low-energy collisions*. Phys. Rev. A **21**, 745 (1980).
- [32] A. Bárány, G. Astner, H. Cederquist, H. Danared, S. Huldt, P. Hvelplund, A. Johnson, H. Knudsen, L. Liljeby, and K.-G. Rensfelt. *Absolute cross sections for multi-electron processes in low energy Arq+Ar collisions: Comparison with theory*. Nuclear Instruments and Methods in Physics Research Section B: Beam Interactions with Materials and Atoms **9**, 397 (1985).
- [33] A. Niehaus. *A classical model for multiple-electron capture in slow collisions of highly charged ions with atoms*. Journal of Physics B: Atomic and Molecular Physics **19**, 2925 (1986).
- [34] J. Burgdörfer and C. Lemell. *Slow Heavy-Particle Induced Electron Emission from Solid Surfaces*, vol. 225 of *Springer Tracts in Modern Physics*, chap. Theoretical

- Concepts and Methods for Electron Emission from Solid Surfaces. Springer Berlin, Heidelberg (2007).
- [35] F. Aumayr, H. Kurz, D. Schneider, M. A. Briere, J. W. McDonald, C. E. Cunningham, and H. Winter. *Emission of electrons from a clean gold surface induced by slow, very highly charged ions at the image charge acceleration limit*. Phys. Rev. Lett. **71**, 1943 (1993).
- [36] J. Burgdörfer and F. Meyer. *Image acceleration of multiply charged ions by metallic surfaces*. Phys. Rev. A **47**, R20 (1993).
- [37] W. Meissl, M. Simon, J. Crespo López-Urrutia, H. Tawara, J. Ullrich, H. Winter, and F. Aumayr. *Highly charged ion-induced potential electron emission from clean Au(111): Dependence on the projectile angle of incidence*. Nuclear Instruments and Methods in Physics Research Section B: Beam Interactions with Materials and Atoms **256**, 520 (2007).
- [38] L. Wirtz, C. O. Reinhold, C. Lemell, and J. Burgdörfer. *Liouville master equation for multielectron dynamics: Neutralization of highly charged ions near a LiF surface*. Phys. Rev. A **67**, 012903 (2003).
- [39] H. Kurz, K. Töglhofer, H. Winter, F. Aumayr, and R. Mann. *Electron emission from slow hollow atoms at a clean metal surface*. Phys. Rev. Lett. **69**, 1140 (1992).
- [40] H. Kurz, F. Aumayr, C. Lemell, K. Töglhofer, and H. Winter. *Neutralization of slow multicharged ions at a clean gold surface: Electron-emission statistics*. Phys. Rev. A **48**, 2192 (1993).
- [41] H. Kurz, F. Aumayr, H. Winter, D. Schneider, M. A. Briere, and J. W. McDonald. *Electron emission and image-charge acceleration for the impact of very highly charged ions on clean gold*. Phys. Rev. A **49**, 4693 (1994).
- [42] G. Holmén, B. Svensson, J. Schou, and P. Sigmund. *Direct and recoil-induced electron emission from ion-bombarded solids*. Phys. Rev. B **20**, 2247 (1979).
- [43] B. Svensson and G. Holmen. *Electron emission from ionbombarded aluminum*. Journal of Applied Physics **52**, 6928 (1981).
- [44] L. A. Dietz and J. C. Sheffield. *Spectrometer for Measuring Secondary Electron Yields Induced by Ion Impacts on Thin Film Oxide Surfaces*. Review of Scientific Instruments **44**, 183 (1973).
- [45] E. Galutschek, R. Trassl, E. Salzborn, F. Aumayr, and H. P. Winter. *Compact 14.5 GHz All-Permanent Magnet ECRIS for Experiments with Slow Multicharged Ions*. Journal of Physics Conference Series **58**, 395 (2007).

- [46] E. Galutschek. *Development of a 14.5 GHz All-Permanent Magnet Multicharged ECR Source for Remote Operation*. Ph.D. thesis, Vienna University of Technology (2005).
- [47] D. Schrempf. *Development of an ultra-compact setup for measuring ion- induced electron emission statistics*. Master's thesis, Vienna University of Technology (2013).
- [48] V. Smejkal. *Design of an electrostatic analyser setup for ion charge state and energy loss analysis after transmission through thin membranes*. Projektarbeit, TU Wien, Institute of Applied Physics (2015).
- [49] J. Ladislav Wiza. *Microchannel plate detectors*. Nuclear Instruments and Methods **162**, 587 (1).
- [50] M. Vana, F. Aumayr, C. Lemell, and H. Winter. *Ion-induced electron emission from solid surfaces: information content of the electron number statistics*. International Journal of Mass Spectrometry and Ion Processes **149-150**, 45 (1995).
- [51] H. Eder, M. Vana, F. Aumayr, and H. P. Winter. *Precise total electron yield measurements for impact of singly or multiply charged ions on clean solid surfaces*. Review of Scientific Instruments **68**, 165 (1997).
- [52] D. Winklehner. *Electron Emission from Insulators upon Impact of Slow Highly Charged Ions*. Master's thesis, Vienna University of Technology (2008).
- [53] Canberra Industries, Inc. https://canberra.com/graphics/content/Literature/Technical_ref/0014cpips05.gif.
- [54] K. Dobes. *Erosion of Fusion Relevant Surfaces under Ion Impact*. Ph.D. thesis, Vienna University of Technology (2014).
- [55] A. H. Castro Neto, F. Guinea, N. M. R. Peres, K. S. Novoselov, and A. K. Geim. *The electronic properties of graphene*. Rev. Mod. Phys. **81**, 109 (2009).
- [56] <https://www.plano-em.de>.
- [57] <http://emresolutions.com>.
- [58] G. Algara-Siller, O. Lehtinen, A. Turchanin, and U. Kaiser. *Dry-cleaning of graphene*. Applied Physics Letters **104**, 153115 (2014).
- [59] ACF-Metals The Arizona Carbon Foil Co., Inc. *PRODUCT INFORMATION 2013*.
- [60] A. Mutzke, R. Schneider, W. Eckstein, and R. Dohmen. *SDTrimSP Version 5.00*. Report IPP 12/8 (2011).

- [61] J. Biersack and L. Haggmark. *A Monte Carlo computer program for the transport of energetic ions in amorphous targets*. Nuclear Instruments and Methods **174**, 257 (1980).
- [62] W. Eckstein. *Computer Simulation of Ion - Solid Interactions*, vol. 10 of *Springer Series in Materials Science*. Springer Berlin, Heidelberg (1991).
- [63] H. Winter, H. Eder, E. Aumayr, J. Lörincik, and Z. Sroubek. *Nucl. In-strum. Meth. Phys. Res. B* **182**, 15 (2001).
- [64] A. Fuchs-Fuchs. Master's thesis, Vienna University of Technology (in prep 2016).
- [65] CAEN Tools for Discovery. *Technical Information Manual MOD. N957 8K MULTI-CHANNEL ANALYZER*, revision n. 5 edn. (2009).
- [66] H. L. Bay, H. H. Andersen, W. O. Hofer, and O. Nielsen. *Transmission sputtering yields of gold at 6.8 MeV*. <http://dx.doi.org/10.1007/BF00897068>.
- [67] W. K. van Asselt, B. Poelsema, and A. L. Boers. *Electron-scattering in a surface-barrier detector*. Journal of Physics D: Applied Physics **11**, L107 (1978).
- [68] L. Rachbauer. *On the automated evaluation of coincident electron emission statistics induced by ion impact on graphene*. Bachelorsthesis, Vienna University of Technology (2016).
- [69] R. Baragiola, E. Alonso, J. Ferron, and A. Oliva-Florio. *Ion-induced electron emission from clean metals*. Surface Science **90**, 240 (1979).
- [70] S. Hippler, D. Hasselkamp, and A. Scharmann. *The ion-induced electron yield as a function of the target material*. Nuclear Instruments and Methods in Physics Research Section B: Beam Interactions with Materials and Atoms **34**, 518 (1988).
- [71] S. Cernusca. *Electron Emission and Nanodefects due to Slow Ion Impact on Solid Surfaces*. Ph.D. thesis, Vienna University of Technology (2003).
- [72] E. Bodewits, R. Hoekstra, K. Dobes, and F. Aumayr. *Electron-emission processes in highly charged Ar and Xe ions impinging on highly ordered pyrolytic graphite at energies just above the kinetic threshold*. Phys. Rev. A **90**, 052703 (2014).
- [73] S. Cernusca, M. Fürsatz, H. Winter, and F. Aumayr. *Ion-induced kinetic electron emission from HOPG with different surface orientation*. EPL (Europhysics Letters) **70**, 768 (2005).
- [74] S. Cernusca, A. Diem, H. Winter, F. Aumayr, J. Lörincik, and Z. Sroubek. *Kinetic electron emission from highly oriented pyrolytic graphite surfaces induced by singly charged ions*. Nuclear Instruments and Methods in Physics Research Section B: Beam Interactions with Materials and Atoms **193**, 616 (2002).

-
- [75] P. M. Echenique, R. M. Nieminen, J. C. Ashley, and R. H. Ritchie. *Nonlinear stopping power of an electron gas for slow ions*. Phys. Rev. A **33**, 897 (1986).
- [76] J. Löriník, Z. Šroubek, H. Eder, F. Aumayr, and H. Winter. *Kinetic electron emission from clean polycrystalline gold induced by impact of slow C^+ , N^+ , O^+ , Ne^+ , Xe^+ , and Au^+ ions*. Phys. Rev. B **62**, 16116 (2000).
- [77] S. Cernusca, H. Winter, F. Aumayr, R. Diez Muiño, and J. Juaristi. *Molecular projectile effects for kinetic electron emission from carbon- and metal-surfaces bombarded by slow hydrogen ions*. Nuclear Instruments and Methods in Physics Research Section B: Beam Interactions with Materials and Atoms **203**, 1 (2003).
- [78] M. Delaunay, M. Fehringer, R. Geller, D. Hitz, P. Varga, and H. Winter. *Electron emission from a metal surface bombarded by slow highly charged ions*. Phys. Rev. B **35**, 4232 (1987).
- [79] S. de Zwart, A. Drentje, A. Boers, and R. Morgenstern. *Electron emission induced by multiply charged Ar ions impinging on a tungsten surface*. Surface Science **217**, 298 (1989).
- [80] V. Smejkal, E. Gruber, R. Wilhelm, L. Brandl, R. Heller, S. Facsko, and F. Aumayr. *A setup for transmission measurements of low energy multiply charged ions through free-standing few atomic layer films*. Nuclear Instruments and Methods in Physics Research Section B: Beam Interactions with Materials and Atoms .
- [81] E. Gruber. *Charge equilibration and energy loss of slow highly charged ions in single layer graphene* (2016).

Danksagung

*Some people can't believe in themselves
until someone else believes in them first.*

- Sean Maguire from Good Will Hunting

An dieser Stelle möchte ich jetzt nun noch die Gelegenheit nutzen, um mich bei all jenen zu bedanken, die wesentlich zum Entstehen dieser Arbeit beigetragen haben.

Zuallererst geht ein sehr großes Dankeschön an meinen Betreuer Prof. Friedrich Aumayr, der mir trotz seiner zahlreichen Verpflichtungen immer wieder genug Zeit einräumen konnte, um mich beim Voranschreiten meiner Arbeit durch wertvolle Ratschläge zu unterstützen. Er hat mir die Möglichkeit geboten meine ersten Erfahrungen in der Wissenschaftswelt zu sammeln und damit bei mir eine Begeisterung geweckt, die ich selbst nie erwartet hätte als ich mit meiner Projektarbeit in seiner Arbeitsgruppe begonnen habe. Durch seine offene Art schafft er eine Arbeitsatmosphäre, die unvergleichlich ist und wesentlich dazu beiträgt immer wieder neue Motivation zu finden, wenn auch einmal nicht alles glatt läuft.

Einen besonderen Dank möchte ich Alexander Fuchs-Fuchs aussprechen, den ich als hervorragenden und besonders geduligen Betreuer während meiner Projektarbeit kennenlernen und als motivierenden Kollegen am Beginn meiner Diplomarbeit genießen durfte. Nie hätte ich ohne dich die Motivation für so viele Nächte und Wochenenden des Messens aufbringen können. Danke, für das Teilen von Momenten der Verzweiflung weil wir zum fünften Mal in Folge unsere Beamline belüften mussten, wie auch der Freude und des Feierns über unsere ersten Koinzidenzspektren. Auch bei allen anderen Kollegen möchte ich mich an dieser Stelle bedanken, da sie alle zu einem einmaligen Arbeitsgruppenklima beigetragen haben, das mich täglich mit viel Freude das Labor betreten ließ. Einige haben sich hier bei mir eine ganz besondere Erwähnung verdient.

Elisabeth Gruber, die mir durch ihren Ehrgeiz und ihre Zielstrebigkeit zu einem wichtigen Vorbild geworden ist. Danke, dass ich bei dir sowohl in fachlichen als auch privaten Angelegenheiten immer Gehör finde. Ich schätze deine Ehrlichkeit und Hilfsbereitschaft und bin froh, dass du während meiner Diplomarbeit zu sehr viel mehr als nur einer Kollegin geworden bist!

Reinhard Stadlmayr, der immer wieder aufs Neue, wenn ich mit einem Problem vor seiner Bürotür gestanden bin, seine unglaubliche Geduld mit mir bewiesen hat. Ein Dankeschön geht auch an Bernhard Berger, der mir durch seine nahezu kindliche Begeisterung für technische Details und sein einzigartiges handwerkliches Geschick eine Menge Zeit und Nerven gespart hat. Danke, dass ihr beide mir immer mit Rat und Tat zur Seite steht!

Paul Szabo, der es geschafft hat mit seiner ruhigen Art immer wieder die richtigen Worte zu finden, um mich vor allem in der hektischen Zeit der Fertigstellung dieser Arbeit vor so mancher Verzweiflung zu bewahren. Ich freue mich schon sehr darauf weiterhin deine Kollegin sein zu dürfen! Florian Laggner, der mit seinem aufgeweckten Gemüt wesentlich zur lockeren Stimmung in der Arbeitsgruppe beiträgt. Danke, dass du es mit Leichtigkeit schaffst mich mit deinen humorvollen Beiträgen immer wieder zum Schmunzeln zu bringen! Mein Dank gebührt auch Lorenz Bergen, der mich beim Schreiben dieser Arbeit immer wieder motivieren konnte! Im Weiteren bedanke ich mich auch bei meinem Bachelorstudenten Lukas Rachbauer für seine aufopfernde Mitwirkung an meiner Diplomarbeit durch das Schreiben eines verlässlichen Auswerteprogramms.

Ein riesengroßes Dankeschön möchte ich auch an meine Freunde aussprechen, die während dieser Zeit viele Hochs und Tiefs mit mir durchgestanden haben. Danke, dass ihr es mir niemals übel genommen habt wenn ich mal wieder zu spät gekommen bin, weil ich doch noch schnell eine Messung beenden musste. Danke, für eure Geduld beim Zuhören jeder noch so langweiligen Laborgeschichte, die für mich in diesem Moment gerade das absolut Wichtigste zu sein schien. Ihr bietet mir die notwendige Abwechslung und schafft es mir immer wieder vor Augen zu führen, welche die wirklich wichtigen Dinge im Leben sind.

Zu guter Letzt möchte ich nun hiermit die Chance ergreifen mich endlich bei meinen Eltern, Isabella und Christian Schwestka, und meiner Schwester, Jennifer Schwestka, für ihre liebevolle Unterstützung in all den Jahren zu bedanken. Ohne euch wäre mein Studium gar nicht erst möglich gewesen. Danke, dass ihr meine Launen während den Prüfungsphasen so gut ausgehalten habt und immer wieder für die doch auch mal nötigen Ablenkungen gesorgt habt. Danke, dass ihr immer für mich da seid und mich bei all meinen Entscheidungen unterstützt!